

Commissioning of the First Insertion Devices on the 1.5 GeV Storage Ring in MAX IV

HAMPUS MÅNEFJORD

DAVID HILL

IN COOPERATION WITH MAX IV LABORATORY

MASTER'S THESIS

DEPARTMENT OF ELECTRICAL AND INFORMATION TECHNOLOGY

FACULTY OF ENGINEERING | LTH | LUND UNIVERSITY



Commissioning of the First Insertion Devices on the 1.5 GeV Storage Ring in MAX IV

Hampus Månefjord, David Hill
hampus.manefjord@gmail.com, davidbzhill@gmail.com

Department of Electrical and Information Technology
Lund University

Supervisor: Hamed Tarawneh, Anders Karlsson

Examiner: Mats Gustafsson

March 5, 2018



Abstract

When installing an insertion device (ID) in a storage ring the electron beam is affected. The positional displacement and angle deflection is called orbit displacement (OD) and higher order effects such as focusing of the electron beam are referred to as linear optics. The ability to perform multiple simultaneous experiments is crucial in a synchrotron light source such as MAX IV. This is impossible to achieve if one ID affects the output of another through the electron beam, making correction for an ID's effect on the beam imperative.

This thesis covers the commissioning process of the first ID to be installed in the MAX IV 1.5 GeV storage ring (R1). The OD and linear optics of an elliptically polarised undulator (EPU) was to be compensated for in a feed forward approach. In essence the commissioning should make the ID transparent to the electron beam.

A general procedure was developed using MATLAB and other software and libraries by first solving the problem on a model of the ring and then in the real storage ring.

The electron orbit was corrected down to $< 1 \mu\text{m}$ for most settings of the ID which is close to the noise level of the measuring system of the ring. The commissioning is considered successful and the ID is ready for beamline delivery and will be able to run without affecting other beamlines.

It was discovered that some magnetic coils performed 25 % below their specifications, and that the beta beat of the bare R1 was at its worst 15 %, something that should be improved for optimal performance of the facility.

Acknowledgements

We would like to offer our greatest gratitude and appreciation to our supervisors Hamed Tarawneh & Anders Karlsson, without you this project wouldn't have been possible. A special thanks to Mihai Pop for sharing his knowledge, office space and humour. You made this project and our time at MAX IV lot more fun. We would also like to thank the rest of the MAX IV staff for their help and patience with us. We have greatly enjoyed the time spent at MAX IV and wish you all the best!

List of Acronyms

AT - Accelerator Toolbox
BPM - Beam Position Monitor
DBA - Double-bend achromat
DH - Downstream Horizontal (used for denoting dipole corrector magnets)
DV - Downstream Vertical (used for denoting dipole corrector magnets)
EPU - Elliptically Polarized Undulator
FFT Feed-forward table
FinEstBeAMS - Finnish and Estonian Beamline for Atmospheric and Material Sciences
GE - General Electric
GUI - Graphical User Interface
ID - Insertion Device
LOCO - Linear Optics from Closed Orbits
MML - MATLAB Middle Layer
OD - Orbit Displacement
ODC - Orbit Displacement Correction
PFS - Pole-face strips
R1 - 1.5 GeV Storage Ring at MAX IV
R3 - 3 GeV Storage Ring at MAX IV
RFI - Residual (magnetic) Field Integral rms - Root Mean Square
SVD - Singular Value Decomposition
SOFB - Slow Orbit Feedback
UH - Upstream Horizontal (used for denoting dipole corrector magnets)
UV - Upstream Vertical (used for denoting dipole corrector magnets)

Table of Contents

1	Introduction	1
2	Background	3
2.1	Synchrotrons	3
2.2	Insertion Devices	3
2.3	MAX IV	6
3	Theory	9
3.1	Definitions	9
3.2	Electromagnetic Radiation	11
3.3	Electron Beam Optics	13
3.4	Correction Strategies	19
4	Methodology	25
4.1	Simulation	25
4.2	Practical implementation	27
5	Results	35
5.1	Magnetic Bench Measurements	35
5.2	Simulated Orbit Correction	36
5.3	Corrector Coils	36
5.4	Orbit Correction and Feed Forward Measurements	37
5.5	Linear Optics Correction	41
5.6	Undulator Light Spectrum	44
6	Discussion	47
6.1	Simulation Accuracy	47
6.2	Magnetic Bench Measurements	47
6.3	Feed Forward Measurement	49
6.4	Higher order correction	50
6.5	Undulator Light Spectrum	50
7	Conclusion	51

A	SVD and QR decomposition	55
B	AT and MML	57
C	Linear Optics from Closed Orbits - LOCO	59

Introduction

Insertion devices (ID's) are devices that convert kinetic energy of relativistic electrons into light in a synchrotron light source such as the MAX IV facility in Lund. In order to take full advantage of such a facility, multiple ID's, or beamlines, are installed on every accelerator ring. This introduces the issue that if one ID distorts the electron beam trajectory, it can affect the output light of all other ID's on the same ring or, in worse cases, cause equipment damage.

The aim of this project is to remove or reduce these distortions using corrector magnets already in place inside the accelerator rings. The distortions caused by an ID depends on its different settings, i.e. its gap distance or phase translation. The main goal of the project is thus to find a generalised method for the creation of a *feed-forward table* (FFT), a table with settings (feed currents) for beam correction magnets that minimises beam disturbances for every setting of the ID.

The targets of these corrections primarily the ID's dipole effects, i.e. the positional and angular displacements of the beam trajectory due to the ID. Secondly the ID's quadrupole effects, i.e. the change of the beam shape due to the ID, was also corrected for. The main criteria for the developed method is that it should be easily adaptable to new IDs and also easily used without any knowledge of the underlying code.

This thesis is a continuation of Sara Mikaelsson's thesis *Commissioning and Characterization of Two Undulators at the MAX IV 3 GeV Storage ring*.^[1] The scope of Mikaelsson's work included commissioning of planar undulators whereas this thesis covers the commissioning of elliptically polarized undulators (EPU's).

As her title suggests, Mikaelsson's work was done at the 3 GeV storage ring (R3) in contrast to the EPUs considered in this thesis, which are placed in the 1.5 GeV ring (R1). Part of Mikaelsson's algorithms and other adaptations made by Mihai Pop at MAX IV will be utilised and used as inspiration when the EPUs are commissioned. However, considerable changes in approach and a complete rewriting of the code was needed in order to complete and generalise the commissioning of the EPUs.

Background

2.1 Synchrotrons

A synchrotron is an accelerator that accelerates particles in a circular trajectory with constant radius.[2] The theoretical basis for the synchrotron light source traces back to 1898 when Liénard derived a formula for a relativistic particle undergoing centripetal acceleration in a circular trajectory. The first practical demonstration was in *General Electrics Research Laboratory* (GE) in 1944, although the experiment was only partially successful as the radiation was never directly observed. In 1947 the first visual observation of synchrotron radiation took place, also at GE.[3]

Since the introduction of the first synchrotron 70 years ago the development has gone through different generations, each outperforming the last by several orders of magnitude. The European Synchrotron Radiation Facility was the first of the third generation synchrotron to operate in 1994.[3] MAX IV is the very first of the new generation of synchrotrons, the fourth generation.[4]

2.2 Insertion Devices

Insertion devices (ID) have a periodic magnetic structure. Usually this is manufactured as an array of permanent magnets with an alternating polarity. When a charged particle traverses the ID longitudinally the charged particle starts to oscillate in the transverse plane. As the particle is accelerated back and fourth transversely, light is emitted. The theoretical groundwork for insertion devices was published in 1947 and experimentally verified in 1953.[3]

There are two types of insertion devices: undulators and wigglers. Undulators are designed in such a way that light emitted from all different periods of oscillation interferes constructively. A well defined wavelength of the light is thus emitted with subsequent harmonics. Wigglers operate at higher fields and fewer magnetic array elements and the result is a wider spectrum with higher flux that extends to shorter wavelengths than that from an undulator.[3]

2.2.1 The Apple II Undulator

The insertion device studied in this work is an elliptically polarised undulator (EPU), the Apple* II design. This design is comprised of purely permanent magnets in four arrays, or blocks with the permanent magnets placed in a pattern of alternating direction which repeats itself after 4 magnets. Each magnet block can be shifted longitudinally to adjust the so called phase of the undulator. If a block is shifted the length of 4 magnets, the resulting magnetic field is the same as at the starting point. This yields the same light production and is referred to as a 360° phase shift.

If two diagonal blocks are moved in unison and the remaining two are stationary, the electron oscillation and produced light goes from vertical linearly polarised at the 0° point to horizontal linearly polarised at the 180° point. At phase points in between, the electron oscillation and produced light are in different states of elliptical polarisation.[5] This type of operational mode is called *helical mode*. In Figure 2.1 the electron trajectory at different phases and the mechanical layout of the Apple II is shown. The motion of the magnetic blocks in helical operational mode is visualised in Figure 2.2.

Figure 2.3 is a photograph of an ID being commissioned outside of the storage ring in MAX IV.

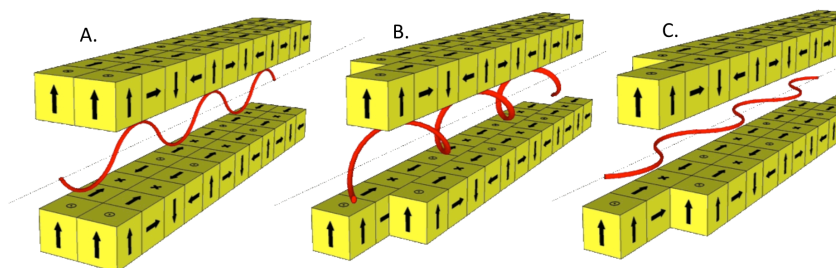


Figure 2.1: A schematic of the magnetic arrays of the Apple II undulator in helical mode at 0° - **A**, 180° - **C** and an intermediate phase - **B**, where an elliptical electron trajectory is seen.[5]

Inclined mode is the other operational mode and is visualised in Figure 2.2. In this mode, the two diagonal magnetic blocks are moved in opposite directions and the remaining are kept stationary. The magnetic field produced from this movement yields no elliptical polarisation. Instead linear polarisation is produced at different angles depending on the phase of the blocks. Again at the 0° point vertical linear polarisation is obtained. At the 180° point, there is horizontal linear polarisation and in between are all other angles of linear polarisation. Both helical and inclined mode is studied in this work.

Besides moving the phase, the so called *gap* of the undulator can be moved. The gap of the undulator is the vertical distance between the magnet blocks and the ideal electron path. The gap can be adjusted by moving the magnetic blocks with

*Advanced Planar Polarised Light Emitter

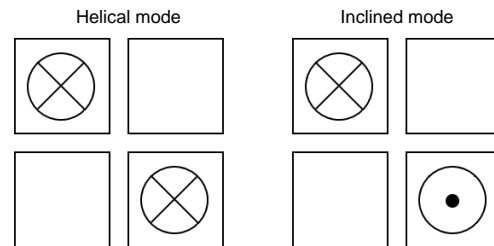


Figure 2.2: A visualisation of how the magnetic blocks move in respect to each other in the different operational modes. The X stand for a movement into the page and the dot toward the reader, the blank blocks are stationary.

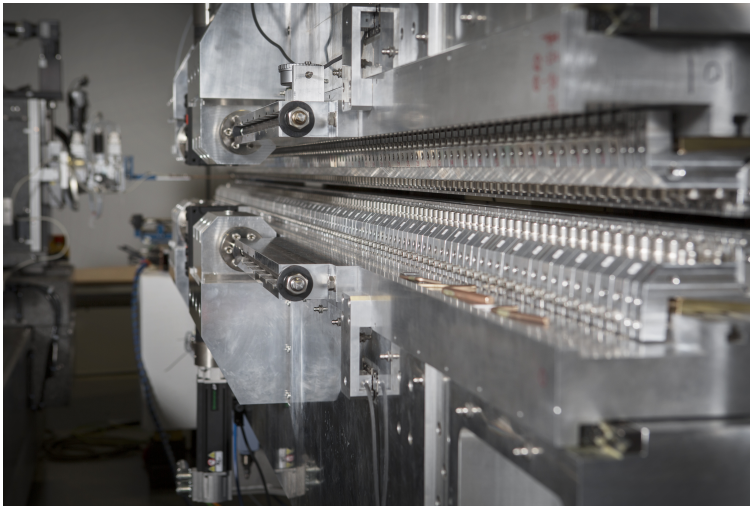


Figure 2.3: A photograph of a MAX IV ID. The permanent magnet array is clearly visible. The ID is not installed in the storage ring in this photo. [6]

stepper motors. When the gap is larger than a threshold value the magnetic blocks do not affect the electron beam as the field strength at the electron path is too weak and can therefore be neglected. This gap is referred to as the maximum gap and is typically around 150 mm. As different gap settings yield different magnetic field strengths, the same device can perform both as an undulator and a wiggler.

2.3 MAX IV

Max IV is a realised world class synchrotron radiation facility hosted by Lund University in Sweden. It is a Swedish national research laboratory and is now considered a role model by other countries.[7, p.7] Figure 2.4 is an aerial photograph of the facility taken in August 2017.



Figure 2.4: Aerial photograph of the facility taken in August 2017 [6].

MAX IV is built on the legacy and experience of 30 years of synchrotron utilisation and development in MAX-lab (MAX I \rightarrow III) in Lund where thousands of users have been offered beam time. During the years the user community has increased from being comprised of roughly 100 physics groups in 1988 to a thousand groups in 2014, equally divided between life sciences, physics and chemistry.[7, p.8]

2.3.1 Beamlines at MAX IV

MAX IV can accommodate 32 beamlines and 25 are planned to be operational by 2026. The individual beamlines utilise different technologies and are used for different purposes and are funded by different sources.[7] The planned beamlines can be seen in Figure 2.5 and the description of beamlines 7, 8 and 9, that are treated in this report, can be read in Table 2.1.

2.3.2 The 1.5 GeV ring, R1

This project solely concerns the smaller of the storage rings, the 1.5 GeV storage ring, internally referred to as R1. The expected brightness of the light produced from R1 is lower than that from the 3 GeV storage ring R3. As a lot of experiments do not need the higher photon energy supplied by R3, the lower energy provided by

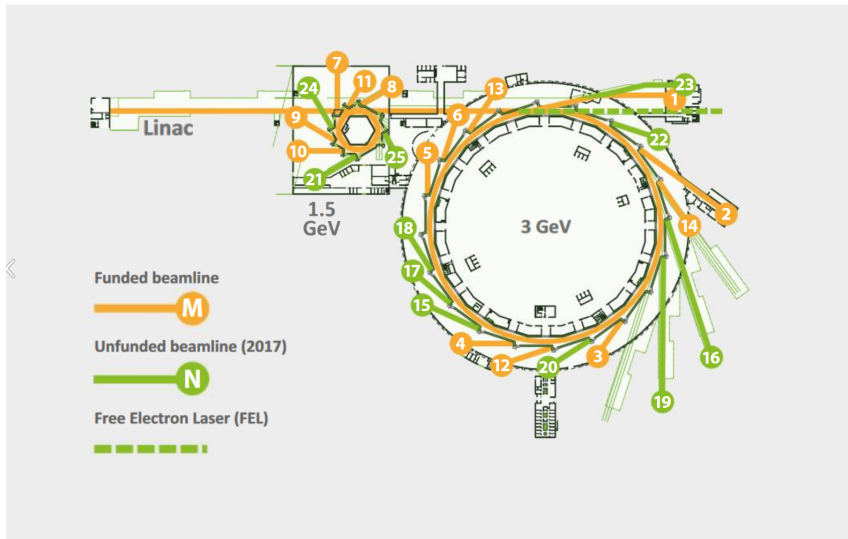


Figure 2.5: The planned beamlines at the MAX IV facility. The yellow beamlines are currently funded whereas the green are not.[7]

R1 is then sufficient. R1 is also planned to allow special operational modes where the time structure of the radiation can be tailored to fit a specific experiment.[7]

The energy of the electrons in R1 is 1.5 GeV. The ring is 96 m in circumference and consists of 12 3.5 m straight sections connected by 4.5 m long double-bend achromats (DBA) in which the electron beam is bent 30° . A schematic outline of one of the 12 DBAs can be seen in Figure 2.6. The horizontally focusing quadrupole elements are visible in red. The blue boxes are the dipole bending magnets. The horizontally defocusing quadrupole magnets are so called pole-face strips (PFS) and are integrated in the dipole magnets [8].

R1 will accommodate beamlines with radiation in the infrared, ultraviolet and X-ray regime. The design of the ring also allows a low emittance with zero dispersion, which is what makes MAX IV such a prominent facility.[8, 3.2.1]

2.3.3 Slow Orbit Feedback System

In both R1 and R3 a so-called slow orbit feedback (SOFB) system is implemented in order to keep the electron orbit the same at all times. Beam position monitors (BPM) measure the transverse position of the beam along the storage ring. With this information the currents in the dipole magnets are adjusted so that the beam is brought as close as possible to a predetermined *golden orbit*. [8, 3.4.6] The system updates at 0.5 Hz and typically manages to bring the orbit to a sub $1 \mu\text{m}$ difference from the golden orbit at each BPM in the straight sections (in the achromat it is not as important and the difference from golden can reach a few μm without it being a problem).

Table 2.1: Descriptions and numberings in figure 2.5 of beamlines treated in this report.[7]

Beamline	No.	Accelerator	Technique
Bloch	7	R1	Angle resolved photoelectron spectroscopy (ARPES) including spin resolution (SPIN ARPES) for studies of the electronic structure of solids and surfaces.
FinEstBeAMS	8	R1	Finnsih and Estonian Beamline for Atmospheric and Material Sciences, electron spectroscopy and luminescence methods for studies of density matter and solids.
SPECIES	9	R1	Resonant inelastic X-ray scattering (RIXS) and near ambient pressure photoemission.

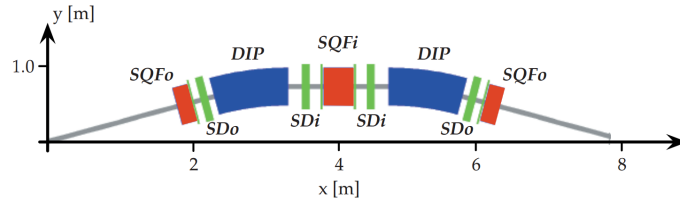


Figure 2.6: Schematic of one of the 12 DBAs of R1. The dipole bending magnets (blue) are flanked by sextupoles (green). There are three combined-function quadrupoles/sextupoles (red). Thin corrector sextupoles are installed throughout the achromat (green, thin). At the grey lines to the sides at $x = 1$ and $x = 7$ are the straight sections flanking the achromat.[8, 3.2.2]

3.1 Definitions

The units used for measuring the magnetic flux (mostly referred to as magnetic field in this thesis) strength is Gauss, which is defined using the SI unit for magnetic flux density, Tesla. [9, p.13]

$$1 \text{ G} = 10^{-4} \text{ T} \quad (3.1)$$

In insertion devices the *residual (magnetic) field integral*, RFI, is often measured in Gcm (Gauss · centimeters).

$$\text{RFI} = \int_L \mathbf{B} \cdot d\mathbf{l} \quad (3.2)$$

$$1 \text{ Gcm} = 1 \cdot 10^{-6} \text{ T m} . \quad (3.3)$$

where \mathbf{B} is the magnetic field and L is the integration path which generally is the electron trajectory through the magnetic field.

The beam divergence and deflection angles treated in this thesis are, when applicable, referred to as "small". The angle θ is considered small if $\sin \theta \approx \theta$, an approximation that is comfortably made for angles of the size 10^{-3} radians ("millirads") or smaller. For an angle of 1 mrad the error in the approximation is on the order of 10^{-10} rad. The deflection angles of the electron beam due to the EPU:s analysed in this thesis are in the order of 10^{-4} rad, or "hundreds of microrads".

The Lorentz factor

$$\gamma = \frac{1}{\sqrt{1 - \beta^2}} = \frac{E_k}{m_0 c^2} \quad (3.4)$$

is the factor by which the relativistic mass, time and distances are altered at relativistic speeds. Here $\beta = \frac{v}{c}$ is the ratio of the speed v to the speed of light c . The right hand side is the kinetic energy divided by the rest energy of the electron, $m_0 c^2$. [10, p.490]

3.1.1 Coordinate system

In accelerator physics several coordinate systems are viable and used in different circumstances. The coordinate system used in the storage ring is an orthonormal

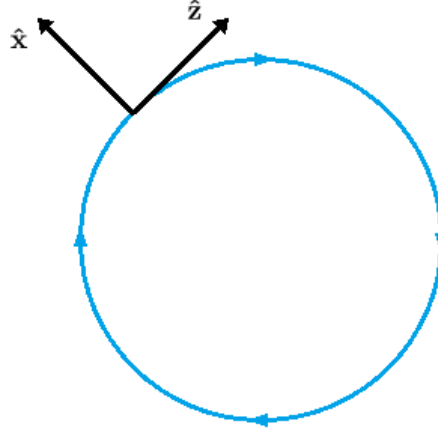


Figure 3.1: Depiction of the Fernet-Serret coordinate system. The blue line is the ideal electron trajectory and \hat{y} is directed out of the page.

basis $(\hat{x}, \hat{y}, \hat{z})$ that is co-moving along the ideal electron beam trajectory.[11, p.47] This is called a Fernet-Serret coordinate system, depicted in Figure 3.1.[9, p.87] The unit vector \hat{z} is always parallel to the ideal beam direction and is constant through straight sections such as corrector magnets and ID:s. The unit vector \hat{x} is defined in the plane normal to \hat{z} and directed out from the centre of the ring. The unit vector \hat{y} is defined as upwards from "the ground" and orthogonal to \hat{x} and \hat{z} . [11] The position coordinate z implies the position along the storage ring, with $z = 0$ at the electron injection point. This coordinate is otherwise often referred to as s in other sources. The coordinates x and y are the distances in \hat{x} and \hat{y} from the ideal trajectory for a given z .

In this thesis the basis *Phase space* is utilised. This is a two- to six-dimensional coordinate basis that gives not only the position but also the direction of the moving particle. Phase space representation of a particle studied in the horizontal plane is then (x, x') where x describes the horizontal position for a given z and x' its horizontal angle to \hat{z} . The complete representation of a particle for a given z is (x, x', y, y') , which for particles in a beam can be further extended with phase and energy spread [9, p.294][11, p.80].

3.1.2 Lorentz Force

The Lorentz force

$$\mathbf{F}_L = q\mathbf{E} + q(\mathbf{v} \times \mathbf{B}) \quad (3.5)$$

is the force \mathbf{F}_L that affects a charge q as it is moving in an electric field \mathbf{E} and magnetic flux density \mathbf{B} [10, p.204].

To change the trajectory of a relativistic charged particle, e.g. an electron, the magnetic field is a more effective tool than the electric field. If the charge velocity is close to the speed of light $v \approx c$ and orthogonal to the magnetic field, $\mathbf{v} \perp \mathbf{B}$, the force from a magnetic field would be $F_M = qcB$ and the electric field

$F_E = qE$. The electric field required to match the force from a 1 T magnetic field is then the unrealistically high $E \approx 300 \text{ MV m}^{-1}$. As a comparison, the electric field where dielectric breakdown of air occurs is around 3 MV m^{-1} [12].

To increase the energy of the charged particle the electric field must be used. Integrating the Lorentz force (Equation 3.5) yields the change in kinetic energy

$$\Delta E_{kin} = \int \mathbf{F}_L \cdot d\mathbf{s} = q \int \mathbf{E} + (\mathbf{v} \times \mathbf{B}) \cdot d\mathbf{s} \quad (3.6)$$

and using that $d\mathbf{s} = \mathbf{v}dt$, the right hand side of Equation 3.6 can be written as

$$q \int \mathbf{E} \cdot d\mathbf{s} + q \int (\mathbf{v} \times \mathbf{B}) \cdot \mathbf{v}dt = q \int \mathbf{E} \cdot d\mathbf{s} . \quad (3.7)$$

The second term on the left hand side is zero according to the definition of cross and dot products. Thereby the magnetic field has no ability to change the energy of a charged particle. [9, p.30]

3.2 Electromagnetic Radiation

Electromagnetic radiation is a direct consequence of the finite speed of light. A charged particle at rest has a static electromagnetic field extending radially towards infinity. Similarly, a charged particle with uniform velocity through space has a radially extending electromagnetic field moving with the same velocity through space. Consider a sudden change in velocity (i.e. an acceleration) of the charged particle, this must result in a change of the electromagnetic field over all space. The information of the velocity change of the particle cannot travel faster than the finite speed of light according to special relativity. Field lines close to the particle point radially out from the particle but outside of the event horizon the field lines still point toward where the particle would have been if the change of velocity had not taken place. As the information of the change travels and the event horizon expands, ripples connecting the conflicting field lines travels with the speed of light. These ripples or distortions of the electromagnetic field lines are known as electromagnetic waves or simply - light. The amplitude of the waves are proportional to the acceleration of the charged particle.[9, p.732]

3.2.1 Synchrotron Radiation

If an acceleration of a charged particle occurs while it is moving close to the speed of light, the properties of the emitted light is affected. This is the case in a synchrotron light source. Due to the doppler effect, a stationary laboratory station perceives a frequency enlarged by a factor 2γ . Due to relativistic Lorentz contraction the frequency increases by another factor γ . [9, p.732] The electron energy in R1 is 1.5 GeV which corresponds to $\gamma \approx 6 \cdot 10^3$ using Equation 3.4.

The radiation pattern of an otherwise stationary particle is a torus (i.e. a dipole radiation pattern). For a dipole travelling with relativistic speeds transversely to the dipole movement, the radiation pattern is transformed into a narrow cone of radiation with a half opening angle of $\frac{1}{\gamma}$. [9, p.733] A schematic of the electromagnetic radiation can be seen in Figure 3.2. This phenomenon increases the

brightness of the radiated light dramatically, which is a reason for the popularity of synchrotron light sources.[11, p.37]

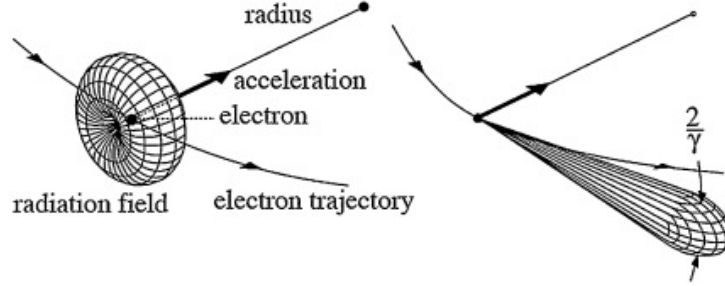


Figure 3.2: To the left is the (dipole) radiation pattern of a relativistic particle within its own frame of reference and to the right is the radiation observed at the laboratory station after a Lorentz transformation of the radiated light.[13]

Insertion devices use the synchrotron radiation phenomenon in order to produce intense and well controlled light by bending the electron trajectory immensely in a very rapid succession. The two paradigms of IDs, i.e. undulators and wigglers, come from how much the electron trajectory is bent over every period of the ID. Undulators bend the beam a little, so little that the transverse speeds v_x and v_y can be wholly neglected. Increasing the magnetic field strength experienced by the electrons, i.e. by decreasing the distance between the magnet arrays of the ID, the transverse speeds cannot be neglected as the electron trajectory wiggles more, giving rise to the name "wigglers". For an undulator, the spectrum is well defined with sharp peaks due to the electrons longitudinal speed matching that of the emitted photons and thus constructive interference occurs. The radiation spectra observed in the longitudinal direction is described by the following equation.

$$\lambda_n = \frac{\lambda_{\text{ID}}}{2n\gamma^2} \left(1 + \frac{K^2}{2} \right) \quad (3.8)$$

λ_n is the wavelength of the n -th harmonic (multiple wavelengths experiences constructive interference), λ_{ID} is the period length or wavelength of the undulators magnetic field. K is the so called *deflection parameter* and is defined as

$$K = \frac{eB\lambda_{\text{ID}}}{2\pi mc} \quad (3.9)$$

with e being the elementary charge, B the magnetic field strength of the undulator, m the mass of the particle (electron) and c the speed of light in vacuum. As can be seen, $K \propto B$ and thus the wavelength of the light produced can be fine-tuned by adjusting the magnetic field strength. Increasing the field strength, i.e. closing the ID gap, leads to the ID entering the wiggler domain where the fine peaks of the undulator spectra is smeared out and a more uniform spectral distribution is achieved. Increasing the field strength also greatly increases the photon flux.[14]

3.3 Electron Beam Optics

In order to control the electron beam trajectory inside the accelerators, multiple steering magnets are used. These magnets interact with the beam in a manner not unlike the interaction of light with optical lenses where both linear and non-linear effects are present. Further similarities to light optics is that the electrons themselves can be modelled as a beam of charge distribution instead of tracking the individual electrons.[11, p.44]

3.3.1 Magnetic Fields

The magnetic flux fields experienced by the electron beam are assumed to be primarily transverse, i.e. $\mathbf{B}(x, y, z) = \hat{\mathbf{x}}B_x(x, y, z) + \hat{\mathbf{y}}B_y(x, y, z)$. As the field does not vary as a function of z , except at the edges of the magnets, the z dependence of B_x and B_y can be neglected. Using multipole expansion the field components can then be expressed as

$$B_x = B_{x0} - \underline{B}_1x + B_1y - \frac{1}{2}\underline{B}_2(x^2 - y^2) + B_2xy + O(u^3) \quad (3.10)$$

$$B_y = B_{y0} + B_1x + \underline{B}_1y + \frac{1}{2}B_2(x^2 - y^2) + \underline{B}_2xy + O(u^3) \quad (3.11)$$

$$u = x \text{ or } y \quad (3.12)$$

where B_0 denotes the dipole component, B_1 the quadrupole component, B_2 the sextupole component etc. [9, p.78] A schematic of the different magnetic components can be seen in Figure 3.3. The $O(u^3)$ is the ordo function which shows the polynomial order of the error of the expansion. The underlined terms correlate to the *skew* components of the field. The skew field components are for the most part unwanted inside the accelerator as they lead to coupling between the x and y position of the beam, which is shown later. The coupling of the terms between the field components B_x and B_y is a result of the requirements $\nabla \cdot \mathbf{B} = 0$ and $\nabla \times \mathbf{B} = 0$, which are derived from Maxwell's equations for the conditions inside the accelerator[11, p.50]. For electromagnets, the strength of the B_i components is controlled by the current running through the coils that produce these fields, generally $B_i \propto I$. [11]

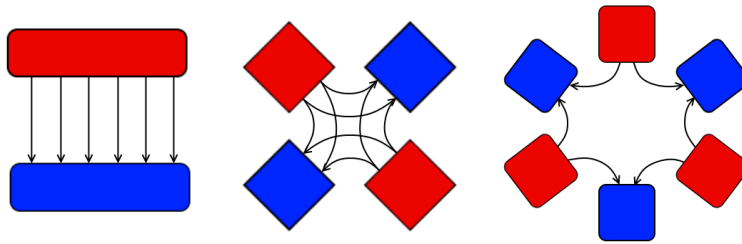


Figure 3.3: A schematic of a dipole to the left, quadrupole in the middle and a sextupole to the right. The red blocks are magnetic north poles and the blue are magnetic south poles. The arrows show where the magnetic field lines are directed.

3.3.2 Magnetic bending equation

The path of the electron beam inside the accelerator is determined by the Lorentz force, Equation 3.5. A relativistic electron with rest mass $m = 9.109\,383\,56 \cdot 10^{-31}$ kg and charge $-e = -1.602\,176\,62 \cdot 10^{-19}$ C [15] moving through the previously discussed transverse field $\mathbf{B} = \hat{\mathbf{x}}B_x(x, y, z) + \hat{\mathbf{y}}B_y(x, y, z)$ with the velocity vector $\mathbf{v} = \hat{\mathbf{x}}v_x + \hat{\mathbf{y}}v_y + \hat{\mathbf{z}}v_z$, where $v_x \ll v_z$, $v_y \ll v_z$, and $v_z \approx c$, has its trajectory bent to follow along a circular orbit with the radii $R_{x,z}$ and $R_{y,z}$. In the x,z-plane, the Lorentz force acts along the radial vector $\hat{\mathbf{r}}_{x,z} = \hat{\mathbf{x}} \cos \theta_x + \hat{\mathbf{z}} \sin \theta_x$, where θ_x is the angle between $\hat{\mathbf{r}}_{x,z}$ and $\hat{\mathbf{x}}$. However, as θ_x is also the angle between $\hat{\mathbf{z}}$ and \mathbf{v} , the approximation $\hat{\mathbf{r}}_{x,z} \approx \hat{\mathbf{x}}$ can be made, provided that $\mathbf{v} \approx \hat{\mathbf{z}}v_z$ holds true. With a similar motivation, $\hat{\mathbf{r}}_{y,z} \approx \hat{\mathbf{y}}$.

The equation describing the beam trajectory bending due to the field is obtained by equating the centripetal force to the Lorentz force, i.e.:

$$\gamma m \mathbf{v}^2 \kappa = -e \mathbf{v} \times \mathbf{B} \approx e(\hat{\mathbf{x}}v_z B_y - \hat{\mathbf{y}}v_z B_x) \quad (3.13)$$

where the curvature is $\kappa = \hat{\mathbf{x}} \frac{1}{R_{x,z}} + \hat{\mathbf{y}} \frac{1}{R_{y,z}}$ [9, p.39]. Equation 3.13 can be further simplified since $\mathbf{v}^2 \approx v_z^2$, and that the momentum of the electrons $p = \gamma m v \approx \gamma m v_z$, which gives the equation

$$p \kappa = e(\hat{\mathbf{x}}B_y - \hat{\mathbf{y}}B_x). \quad (3.14)$$

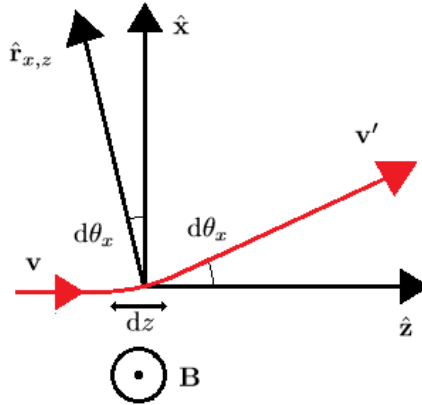


Figure 3.4: Small deflection of electron trajectory due to a magnetic field $\mathbf{B} = \hat{\mathbf{y}}B_y(x, y)$. $R_{x,z}$ can be seen as the length of $\hat{\mathbf{r}}_{x,z}$ and the deflection angle $d\theta_x$ is greatly exaggerated.

In order to investigate how a magnetic field affects the trajectory of the electrons, consider the situation depicted in Figure 3.4 where a magnetic field is acting only along the y-axis, $\mathbf{B} = \hat{\mathbf{y}}B_y(x, y, z)$, and nonzero for only a short interval dz . An electron initially travelling with the velocity vector \mathbf{v} enters the field and travels the small distance $dl \approx dz$. When passing through the field, the electron's

velocity vector is changed from \mathbf{v} to \mathbf{v}' by the angle $d\theta_x = \theta'_x - \theta_x$. Special for the case in Figure 3.4 is that $\theta_x = 0$ as $\mathbf{v} = \hat{\mathbf{z}}v_z$, but this is not a general requirement. As $d\theta_x$ is small, the relation

$$d\theta_x \approx \sin d\theta_x = \frac{dz}{R_{x,z}} = \frac{e}{p}B_y dz \quad (3.15)$$

can be established by rewriting $R_{x,z}$ using Equation 3.14. Generalising this result to a magnetic field that is nonzero for $z \in [z_0, z_0 + l_m]$ and integrating along the electron trajectory gives the total deflection as

$$\theta_x = \frac{e}{p} \int_{z_0}^{z_0+l_m} B_y(x, y, z) dz = \frac{e}{p} \text{RFI}_y, \quad (3.16)$$

given that the total deflection θ_x still can be considered small, i.e. that $v_x \ll v_z$ holds for all $z \in [z_0, z_0 + l_m]$.

In a similar manner, the deflection in the y-direction is given from a magnetic field $\mathbf{B} = \hat{\mathbf{x}}B_x(x, y, z)$ as

$$\theta_y = -\frac{e}{p} \int_{z_0}^{z_0+l_m} B_x(x, y, z) dz = -\frac{e}{p} \text{RFI}_x. \quad (3.17)$$

3.3.3 Dipole Magnet Bending

The simplest magnet used to steer the beam is the dipole magnet which ideally only produces the dipole field components in Equations 3.10 and 3.11, i.e. $B_y(x, y) = B_{y0}$ for bending in the horizontal plane and $B_x(x, y) = B_{x0}$ for bending in the vertical plane. The deflection angles of Equations 3.16 and 3.17 are then simplified to

$$\theta_x = \frac{e}{p} B_{y0} l_m \quad (3.18)$$

$$\theta_y = -\frac{e}{p} B_{x0} l_m \quad (3.19)$$

3.3.4 Quadrupole Magnet Focusing

A quadrupole magnet ideally only produces the quadrupole field components from Equations 3.10 and 3.11 and thus has the magnetic field $\mathbf{B} = \hat{\mathbf{x}}(-\underline{B}_1 x + B_1 y) + \hat{\mathbf{y}}(B_1 x + \underline{B}_1 y)$. Simplified from 3.16 and 3.17, the deflection angles now become

$$\theta_x = \frac{e}{p} (B_1 x + \underline{B}_1 y) l_m \quad (3.20)$$

$$\theta_y = -\frac{e}{p} (-\underline{B}_1 x + B_1 y) l_m \quad (3.21)$$

which, as seen from their expressions, depends on the displacements x and y of the electrons' trajectory from the centre of the quadrupole field. What also can be seen is the effect of the skew field components. When $\underline{B}_1 \neq 0$ a trajectory displacement in y propagates to a displacement in x , which is bad. From here

on, the magnets used are assumed to be ideal without skew components. The deflections from the quadrupole magnets then are

$$\theta_x = \frac{e}{p} B_1 x l_m \quad (3.22)$$

$$\theta_y = -\frac{e}{p} B_1 y l_m \quad (3.23)$$

An important note from this is that as the field amplitudes in \hat{x} and \hat{y} are coupled through B_1 , the magnet causes, depending on the sign of B_1 , a diverging deflection along one axis and a converging deflection along the other axis - but never converging in both axes at the same time.

The focal lengths f_x and f_y of a quadrupole magnet is given by the relations [9, p.42]

$$\theta_x = -\frac{x}{f_x} \quad (3.24)$$

$$\theta_y = -\frac{y}{f_y} \quad (3.25)$$

which combined with equations 3.22 and 3.23 yield

$$f_x^{-1} = -\frac{e}{p} B_1 l_m \quad (3.26)$$

$$f_y^{-1} = \frac{e}{p} B_1 l_m . \quad (3.27)$$

From this the so called *focusing strength* of the quadrupole magnet is defined as

$$k = \frac{e}{p} B_1 . \quad (3.28)$$

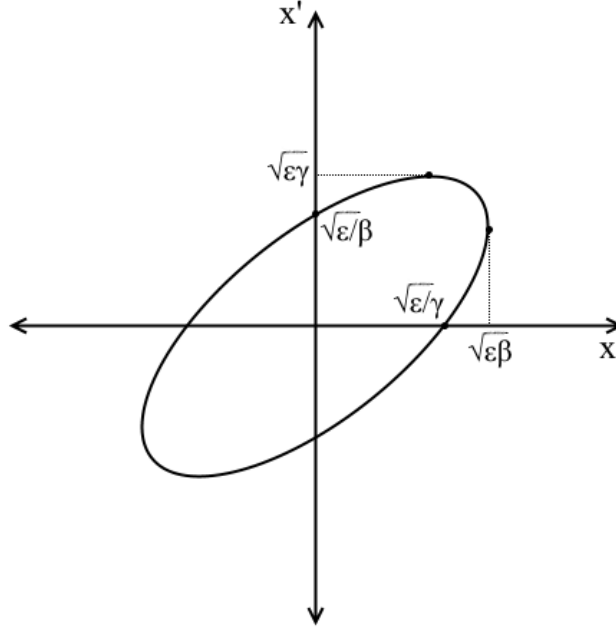


Figure 3.5: The phase ellipse at an arbitrary z -position z_A with its half axes and extreme values marked out in the figure. ε is the emittance, β refers to $\beta(z_A)$ and $\gamma = \gamma(z_A) \propto \frac{1}{\beta(z_A)}$ is another of the so called twiss parameters that defines the beam.[11, p.80] Note: At z_A the beam is diverging which is easily seen as positive x -positions also have a positive angle x' .

3.3.5 Linear Beam Optics

As stated, instead of analysing every electron individually it is advantageous to find a way to describe the electrons as a beam in a similar manner to photonic beam optics. Since the accelerator consists of a periodic structure of magnets, the path of the electron beam is described by Hill's differential equation of motion*. For an electron beam only affected by quadrupole fields, Hill's equation reads[11, p.77][9, p.249]:

$$x''(z) - \frac{e}{p} B_1(z)x(z) = 0 \quad (3.29)$$

with the solution [11, p.78]

$$x(z) = \sqrt{\varepsilon_x} \sqrt{\beta_x(z)} \cos(\Psi_x(z) + \phi). \quad (3.30)$$

Here ε_x is the *emittance* in x , $\beta_x(z)$ is the *beta function* (or amplitude function) in x , the phase is

$$\Psi_x(z) = \int_0^z \frac{1}{\beta_x(\sigma)} d\sigma \quad (3.31)$$

*No connection to the author of this thesis.

and ϕ is a constant that depends on the initial conditions.

The *tune* Q is an important design parameter in storage rings defined as

$$Q \equiv \frac{\Psi(z + C) - \Psi(z)}{2\pi} \quad (3.32)$$

where C is the circumference of the storage ring, i.e. the tune is the total phase advancement of a particle after one revolution in the ring. There are a lot of resonances in the tune that have to be avoided when designing the accelerator.[11, p.101]

Investigation of the z -derivative of x in Equation 3.30 shows that x and x' define an ellipse in phase space (i.e. (x, x') , see Section 3.1.1) with halfaxes and orientation that depend on the position z , see Figure 3.5. The ellipse has the area $A = \pi\varepsilon$ independently of z and its shape defines the transverse confinement of the electrons inside the beam. An arbitrary electron inside the accelerator at the point z_0 with its phase space coordinates confined by this ellipse continues to be confined for any z , even as the ellipse changes shape[11, p.80][9, p.154]. An envelope function $E(z) = \sqrt{\varepsilon_x \beta_x}$ can from this be derived for x which determines the physical width of a beam that contains all electrons constrained by the (x, x') ellipse in phase space. A visualisation of this envelope function can be seen in Figure 3.6. In order to study how a beam of many electrons traverse the accelerator only the position x and divergence x' of the electrons on the boundary of the phase ellipse need to be analysed.

The beta function also influences the positional displacement of the closed orbit beam due to a dipole deflection. Inserting a dipole magnet acting with the deflection angle θ_x (Equation 3.18) at the point z_0 in the ring changes Hill's differential equation (Equation 3.29) to

$$x''(z) - \frac{e}{p} B_1(z)x(z) = \delta(z - z_0)\theta_x . \quad (3.33)$$

Solving this by seeing the dipole deflection as a perturbation yields the solution [16]

$$x(z) = \frac{\sqrt{\beta(z)\beta(z_0)}}{\sin \pi Q} \theta_x \cos(\pi Q - \Psi_x(z) + \Psi_x(z_0)). \quad (3.34)$$

This solution also shows one of the tune resonances that are avoided when designing the accelerator: if Q is an integer the orbit blows up. This can be physically interpreted, consider an electron with an integer tune being kicked by a dipole magnet. The electron is kicked at the exact same position within its oscillation each lap of the storage ring. The displacements from these kicks adds up and excite the electron orbit past set boundaries leading to a beam dump.

Another effect of magnetic dipoles on the beam is the so called *dipole edge effect* or *dipole focusing phenomena*. This comes from when two electrons inside a beam have different path lengths inside a dipole and thus experiences different angle deflections. This leads to a focusing effect that increases with the size of the beam.

As the 1.5 GeV ring lattice at MAX IV is designed to be periodic and symmetric, the beta function is also periodic. The designed beta function of an achromat

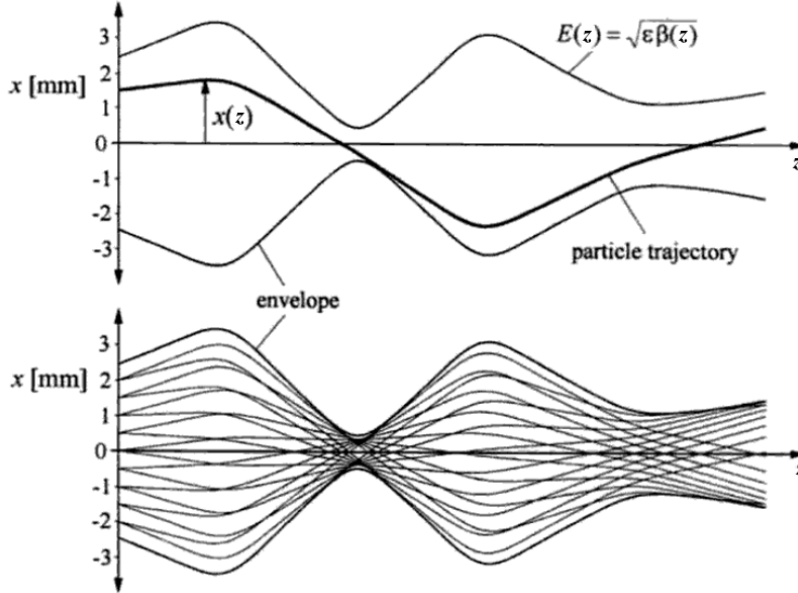


Figure 3.6: The envelope function $E(z)$ in \hat{x} along a portion of the storage ring. A single electron trajectory $x(z)$ constrained by the envelope is shown in the upper figure while 18 different trajectories are shown in the lower figure.[11, p.79]

in R1 can be seen in Figure 3.7. The IDs disturb this periodicity and symmetry due to an intrinsic focusing. The focusing is a consequence of the beam traversing the periodic magnetic field inside the ID, focusing the beam in a similar manner to dipole edge focusing. In practice the RFI of the quadrupole field will also not be perfectly zero, adding a small quadrupole focusing due to imperfections in the ID. The total focusing effect can be expressed as a quadrupole field and induces a so-called *betatron beat*, or in short - beta beat. The beat is a measure of how much the current beta function has strayed from the design beta function β_0 , i.e. $\frac{\Delta\beta}{\beta_0}$ and is usually given in percent.[9, p.524] As the beta function changes, the tune of the machine shifts (Equation 3.32) which is disastrous if the tune drifts too close to one of the many resonances of the machine. For this reason, the ID's quadrupole beam shaping effect needs to be corrected for in addition to the ID's dipole orbit displacement effect.

3.4 Correction Strategies

The strategies for counteracting the insertion device effects on the electron beam entails working with one error at the time. First the orbit's displacement is corrected using the four dipole corrector magnets flanking the ID, i.e. counteracting the ID's dipole component. After this the two closest focusing quadrupoles and

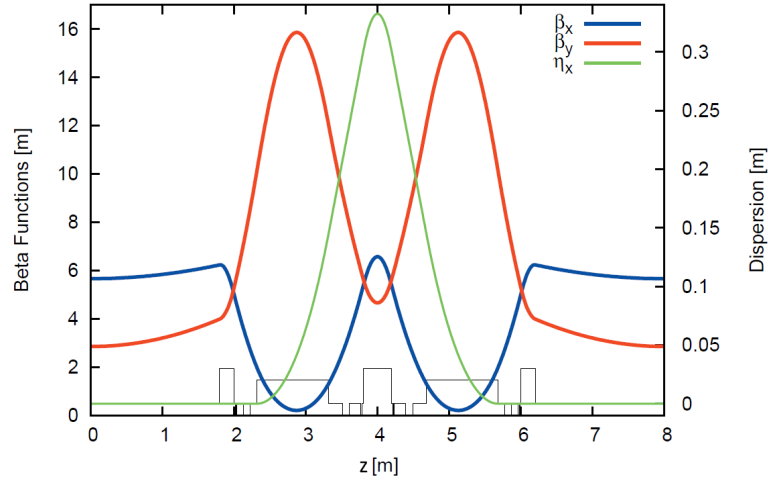


Figure 3.7: The designed beta and dispersion functions in one of the R1 achromats. In blue is the horizontal beta function, in red the vertical beta function. In green is the dispersion function and the positions of the magnets in the achromat (see Figure 2.6) is indicated in the bottom in black.[8]

the two closest PFS's eliminate the ID's quadrupole effect, reducing the beta beat and tune shift. If this is insufficient, all quadrupoles and PFS's along the ring can be used. Finally, the ID's sextupole effect can be counteracted by using sextupole corrector magnets which will reduce higher order errors in the beam.

3.4.1 Orbit displacement correction

The effect of the undulator on the orbit is detectable from the BPMs that are dispersed throughout the ring. An orbit is denoted by the column vector $\Omega = [\mathbf{x}, \mathbf{y}]^T$, where every value in the row vectors \mathbf{x} and \mathbf{y} corresponds to the x and y beam position readings from different BPMs in the ring. For an initial orbit Ω_0 (i.e. the golden orbit to be corrected back to) the orbit is shifted to Ω_{ID} after introducing the disturbance originating from the intrinsic effect of the ID. The orbit displacement (OD) due to the ID can then be written as

$$\Delta\Omega_{ID} = \Omega_{ID} - \Omega_0 \quad (3.35)$$

In a similar manner, the orbit displacement away from the initial orbit induced by the corrector magnets is denoted as $\Delta\Omega_{CM}$. The strategy to return to the initial orbit Ω_0 is simply to change the currents in the corrector magnets such that

$$\Delta\Omega_{ID} + \Delta\Omega_{CM} = 0 \quad (3.36)$$

is fulfilled.

The effect of the corrector magnets on the orbit is modelled using the response

matrix

$$\mathbf{R} = \begin{bmatrix} \mathbf{R}_{xx} & \mathbf{R}_{xy} \\ \mathbf{R}_{yx} & \mathbf{R}_{yy} \end{bmatrix} = \begin{bmatrix} \frac{\partial x_1}{\partial I_{\text{HU}}} & \frac{\partial x_1}{\partial I_{\text{HD}}} & \frac{\partial x_1}{\partial I_{\text{VU}}} & \frac{\partial x_1}{\partial I_{\text{VD}}} \\ \frac{\partial x_2}{\partial I_{\text{HU}}} & \frac{\partial x_2}{\partial I_{\text{HD}}} & \frac{\partial x_2}{\partial I_{\text{VU}}} & \frac{\partial x_2}{\partial I_{\text{VD}}} \\ \vdots & \vdots & \vdots & \vdots \\ \frac{\partial x_n}{\partial I_{\text{HU}}} & \frac{\partial x_n}{\partial I_{\text{HD}}} & \frac{\partial x_n}{\partial I_{\text{VU}}} & \frac{\partial x_n}{\partial I_{\text{VD}}} \\ \frac{\partial y_1}{\partial I_{\text{HU}}} & \frac{\partial y_1}{\partial I_{\text{HD}}} & \frac{\partial y_1}{\partial I_{\text{VU}}} & \frac{\partial y_1}{\partial I_{\text{VD}}} \\ \frac{\partial y_2}{\partial I_{\text{HU}}} & \frac{\partial y_2}{\partial I_{\text{HD}}} & \frac{\partial y_2}{\partial I_{\text{VU}}} & \frac{\partial y_2}{\partial I_{\text{VD}}} \\ \vdots & \vdots & \vdots & \vdots \\ \frac{\partial y_n}{\partial I_{\text{HU}}} & \frac{\partial y_n}{\partial I_{\text{HD}}} & \frac{\partial y_n}{\partial I_{\text{VU}}} & \frac{\partial y_n}{\partial I_{\text{VD}}} \end{bmatrix}. \quad (3.37)$$

\mathbf{R} is the Jacobian of $\boldsymbol{\Omega}$ with n BPMs as a function of the corrector magnet coil currents $\mathbf{I} = (I_{\text{HU}}, I_{\text{HD}}, I_{\text{VU}}, I_{\text{VD}})$ where HU, HD, VU and VD denote the deflection direction (horizontal and vertical) and position (upstream and downstream) of the corrector magnets. The submatrices \mathbf{R}_{xx} and \mathbf{R}_{yy} are the normal components. They measure the horizontal displacement at the BPMs resulting from a kick from the corrector magnet in the horizontal plane. The off-diagonal submatrices \mathbf{R}_{xy} and \mathbf{R}_{yx} are the so-called skew components. These skew components are a measure of the magnitude of vertical displacement of the electron beam arising from a horizontal kick by a corrector magnet, and vice versa. The storage rings are designed to keep the coupling i.e. the skew components close to zero. High values in these skew matrices then show that either the ID has a strong skew component field or that the accelerator ring itself is erroneous.

\mathbf{R} can be numerically obtained by exclusively changing the current of every corrector magnet coil by $\pm\Delta I/2$, which results in a small orbit displacement $\Delta\boldsymbol{\Omega}_k = \boldsymbol{\Omega}(I_k = +\Delta I/2) - \boldsymbol{\Omega}(I_k = -\Delta I/2)$ where $k = \text{HU}, \text{HD}, \text{VU}, \text{VD}$. By utilising central difference approximation \mathbf{R} is the numerical derivative

$$\mathbf{R} = \begin{bmatrix} \frac{\Delta\boldsymbol{\Omega}_{\text{HU}}}{\Delta I} & \frac{\Delta\boldsymbol{\Omega}_{\text{HD}}}{\Delta I} & \frac{\Delta\boldsymbol{\Omega}_{\text{VU}}}{\Delta I} & \frac{\Delta\boldsymbol{\Omega}_{\text{VD}}}{\Delta I} \end{bmatrix} \quad (3.38)$$

Assuming that the orbit displacement $\Delta\boldsymbol{\Omega}_{\text{CM}}$ depends linearly on the current changes $\Delta\mathbf{I} = [\Delta I_{\text{HU}}, \Delta I_{\text{HD}}, \Delta I_{\text{VU}}, \Delta I_{\text{VD}}]^T$ then

$$\Delta\boldsymbol{\Omega}_{\text{CM}} = \mathbf{R}\Delta\mathbf{I}. \quad (3.39)$$

holds for currents within the limitations of the corrector magnets. Insertion of Equation 3.39 into 3.36 gives

$$\mathbf{R}\Delta\mathbf{I} = -\Delta\boldsymbol{\Omega}_{\text{ID}}. \quad (3.40)$$

which in turn yields the current changes needed to counteract the orbit displacement due to the ID if solved for $\Delta\mathbf{I}$.

3.4.2 Saturated correction coil orbit correction

Realistically the corrector magnet coils cannot sustain any given current without being overheated. The currents through the coils are thus restricted by some

maximum current I_{max} , determined by the limits of the magnet power supplies and the coils' heat resistance. If the orbit correction strategy already discussed would lead to a new current $I_k = I_{kprevious} + \Delta I_k$, $|I_k| > I_{max}$ the coil would be saturated and the solution given by Equation 3.40 cannot be applied. In order to still achieve some correction in such a case the other corrector magnet active in the same plane, i.e. vertical or horizontal, has to weigh up for the saturated coil.

Assuming no skew coupling and viewing only the horizontal corrector magnets, Equation 3.40 is reduced to

$$\mathbf{R}_{xx}\Delta\mathbf{I}_H = -\Delta\mathbf{x}_{ID} . \quad (3.41)$$

If it is the upstream corrector that is saturated after solving 3.40 then the current for the upstream horizontal corrector coil is instead set as $I_{HU} = \text{sign}(I_{HU})I_{max}$. This gives the difference $\Delta I_{HU} = I_{HU} - I_{HU\text{initial}}$, removing one unknown from the system of equations stated in Equation 3.41. Splitting \mathbf{R}_{xx} into two column vectors

$$\mathbf{R}_{xx} = [\mathbf{R}_{xxU} \quad \mathbf{R}_{xxD}] \quad (3.42)$$

an equation for the remaining ΔI_{HD} can be constructed

$$\mathbf{R}_{xxD}\Delta I_{HD} = -\Delta\mathbf{x}_{ID} - \mathbf{R}_{xxU}\Delta I_{HU}. \quad (3.43)$$

Solving this for ΔI_{HD} yields the correction to the displacement $\Delta\mathbf{x}_{ID}$. If another corrector than the above example is saturated a similar scheme can be constructed to obtain the relevant current.

3.4.3 Linear Optics Correction

After correcting the orbit displacement, the ID's residual quadrupole field can be addressed. In theory this can be done in a similar manner as for the orbit correction but instead of calculating the dipoles' effect on the orbit, the quadrupole magnet coil currents' effects on the tune and beta function are determined. In practice the beta function cannot be measured directly and correcting only for the tune is prone to error as it is a single point measurement. Instead the LOCO algorithm, see Appendix C, is used to fit a model of the ring without any distortion from the ID (the ID is at max gap) to the real machine with the ID active (ID at a closed gap).

The strategy for correcting the linear optics with LOCO is summarised in Figure 3.8. Starting with an *initial model* of the machine based on the machine design, an *open gap model* is constructed by changing all quadrupole magnet strengths in the initial model using LOCO to match machine measurements at open gap (LOCO step 1 in Figure 3.8). This is done to get the best possible model of the real machine's actual linear optics. The open gap model is also a model of the state that the real machine is to be returned to.

After obtaining the open gap model, LOCO is used a second time, changing some quadrupole magnets to match the open gap model with measurements of the real machine at closed gap (LOCO step 2 in Figure 3.8). Comparing the open gap model to the closed gap model, the only difference of the two are the strengths of some quadrupole magnets. This difference is equivalent to closing the ID, and

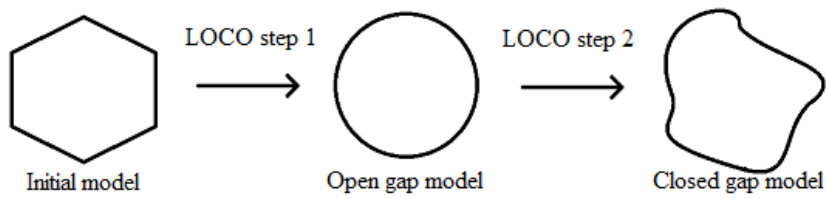


Figure 3.8: Graphical summary of the linear optics correction method using LOCO. Starting with an initial design model, two new models are obtained where the difference of the two yields the correction necessary to mend the linear optics.

thus, applying this difference in reverse on the real machine should counteract the IDs quadrupole effect. The choice of the magnets used for correction is done when choosing which quadrupole magnets to do the fitting with in LOCO step 2.

4.1 Simulation

4.1.1 Simulation of R1

The MATLAB toolboxes *Accelerator Toolbox*[17], AT, and *Matlab Middle Layer*[18], MML (see Appendix B), were used to model and analyse the bare structure of the 1.5 GeV storage ring, R1. Such a model structure is called a lattice. In the bare lattice a straight section was extracted and replaced with a model of an ID and corrector magnets in both transverse planes up- and downstream of the ID. The lattice with the three inserted IDs can be seen in Figure 4.1. By changing the values of the dipole and quadrupole elements integrated in the model ID, different gap settings were simulated.

4.1.2 Simulation of the Insertion Devices

The insertion devices were modelled with different magnetic components added in AT that represent the residual magnetic field integral of the ID. Two zero-length dipoles were placed at $z = z_0 + \frac{l_m}{4}$ and $z = z_0 + \frac{3l_m}{4}$ (upstream and downstream), where the ID spans $z = [z_0, z_0 + l_m]$. A 15 cm long quadrupole magnet was placed at $z = z_0 + \frac{l_m}{2}$. The input to each of the dipoles in AT was the deflection angles calculated using Equations 3.16 and 3.17. The angles were calculated from an upstream RFI of 300 Gcm in both x and y and a downstream RFI of -100 Gcm. The total dipole RFI was then 200 Gcm.

The input to the quadrupole in AT is the focusing strength k from Equation 3.28, which was set to $k = 0.06 \text{ m}^{-1}$ in the model. This value corresponds to the multipole coefficient $B_1 = 30 \text{ G/cm}$ for R1 electrons. These parameters were suggested by supervisor Hamed Taranweh, who has vast experience in dealing with IDs.

4.1.3 Simulated orbit displacement correction

After the simulated IDs had been added to the lattice the orbit correction strategy discussed in the previous chapter was implemented. The response matrix \mathbf{R} from Equation 3.37 was calculated by changing the corrector magnet divergence angles. For the simulations little to no coupling between the horizontal orbit to

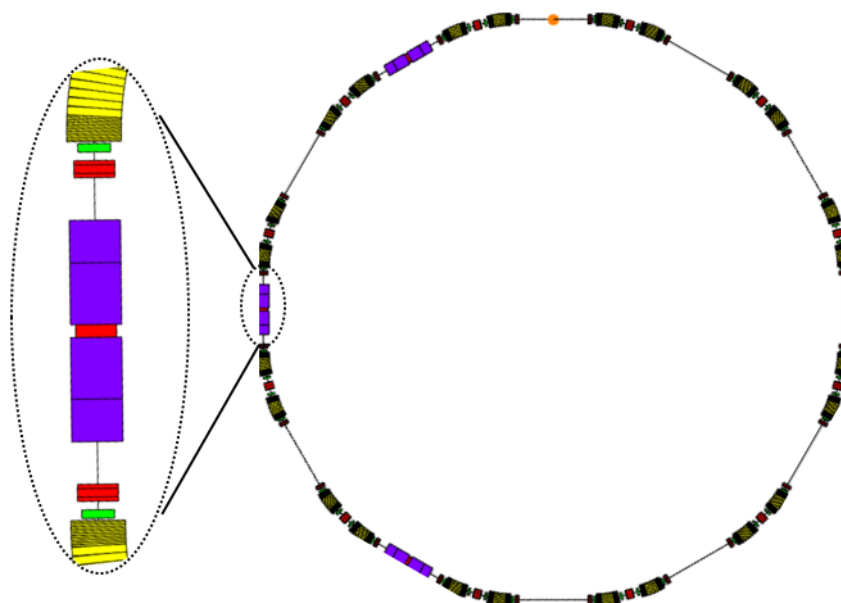


Figure 4.1: To the left is a closeup on one of the IDs in the AT lattice. The yellow blocks are the bending magnets, the red blocks are quadrupoles, green is the SDI and the purple block is the ID. The black lines dividing each purple block in two correlate to the position of the horizontal and vertical kicker. To the right is the complete lattice of R1 with 3 undulators, the insertion point is marked with an orange circle.

the vertical corrector magnets, and vice versa, was assumed - i.e. \mathbf{R}_{yx} and \mathbf{R}_{xy} are either zero-valued or contain much smaller values than \mathbf{R}_{xx} and \mathbf{R}_{yy} . After a method comparison (see appendix A) between MATLABs integrated QR-solver [19] and the SVD method used by Sara Mikaelsson, Equation 3.40 was solved using MATLABs integrated QR-solver.

4.1.4 Simulated linear optics correction

As the ID was simulated with a quadrupole effect, the linear optics of the simulated lattice was also affected. As the beta function and tune is known inside AT for all z along the lattice, response matrices for the flanking quadrupoles' effect on the beta beat and tune could be constructed and used to correct both the tune drift and beta beat of the lattice due to the ID's effects. The response matrices and corrections were made using the AT function `fittune2`. From Equation 3.32 it can be reasoned that correcting the tune also corrects the beta beat. The aim of these correction simulations were to compare them to the correction accomplished by the LOCO method, which was implemented in accordance with how it is described in Section 3.4.3.

Two implementations of the LOCO correction were made. One using the

quadrupoles and PFS's that are directly flanking the ID and the other implementation does the LOCO correction using all quadrupoles and PFS's in R1.

4.1.5 Simulation of the Undulator Light

A software called Spectra[20] was used to simulate the radiation produced from the FinEstBeAMS ID in R1. The parameters of both the ring and the ID was taken into consideration in the software from which the expected spectrum and energy flux was calculated.

4.2 Practical implementation

The software package Tango[8, 2.9] was used to handle the communication between the software and the hardware. Libraries such as *Matlab Middle Layer*, MML, and Tango Matlab Bindings[21] were in turn utilised to communicate between MATLAB and TANGO.

The first machine to be commissioned was FinEstBeAMS, started on the 13th of November 2017.

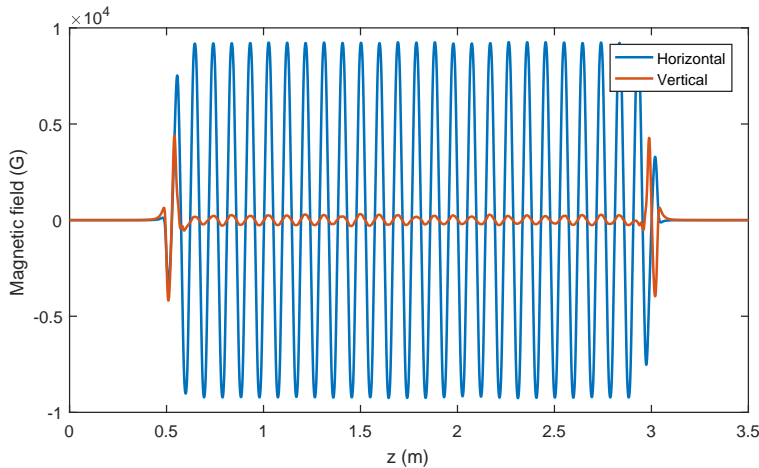


Figure 4.2: The magnetic field inside FinEstBeAMS measured when the device is in vertical mode (*helical*, phase = 47.6 mm gap = 14.2 mm). Vertical in this case refers to the light produced. The main component of the magnetic field is directed horizontally (blue). The magnetic field and polarisation of the light will always be orthogonal to each other due to the Lorentz force, Equation 3.5.

4.2.1 Magnetic Bench Measurements

The magnetic field inside the ID was characterised by the *Insertion Device Team* at MAX IV prior to installation with a so-called magnetic bench measurement using a

Hall probe and a wire scan. The magnetic field longitudinally along FinEstBeAMS was mapped and is shown for vertical polarisation in Figure 4.2 and for horizontal polarisation in Figure 4.3.

Integration of the magnetic field strengths visualised in Figures 4.2 and 4.3 yields the RFI. The RFI can more easily be measured using a wire scan. This was done for different x positions with $y = 0$, and the corresponding measurements are shown in Figures 4.4 and 4.5 for the vertical and circular field respectively. In these figures, a polynomial fit has been made with large weights on data points close to $x = 0$. These weights were chosen as the beam will be confined to a small area around $x = y = 0$. As the data in these figures correspond to $\int B_x(x, 0, z)dz = \text{RFI}_x$ and $\int B_y(x, 0, z)dz = \text{RFI}_y$, the integrated multipole components of the ID is obtained by matching the terms in Equations 3.10 and 3.11 to the calculated polynomial terms. Other than the data shown in Figures 4.4 and 4.5, the field components of the inclined and horizontal mode was also calculated. The mode names refer to the produced light polarisation where the horizontal mode is defined as phase = 0 mm and gap = 14 mm. The inclined mode (linear polarisation tilted 45°) is defined as phase = 25.4 mm and gap = 15.4 mm.

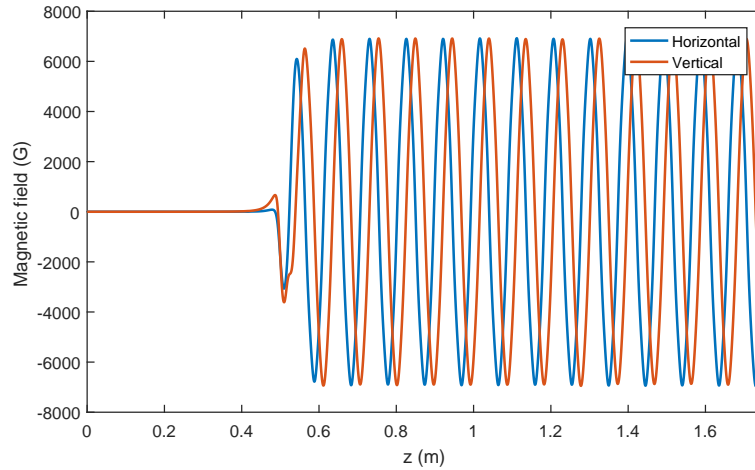


Figure 4.3: The x and y components of the magnetic field inside FinEstBeAMS measured when the device is in circular mode (*helical*, phase = 27 mm gap = 15.4 mm). Notice that the amplitude of the horizontal and vertical field are equivalent but out of phase, a characteristic that will produce circularly polarised light. In this plot only half of the ID is included, so as to make it easier for the reader to see the phase difference. The magnetic field inside the ID is mirror symmetric in z .

4.2.2 Corrector response time measurements

The Tango Matlab bindings were used to test the corrector coils. A current change was written to the corrector magnets and the response time was measured. The

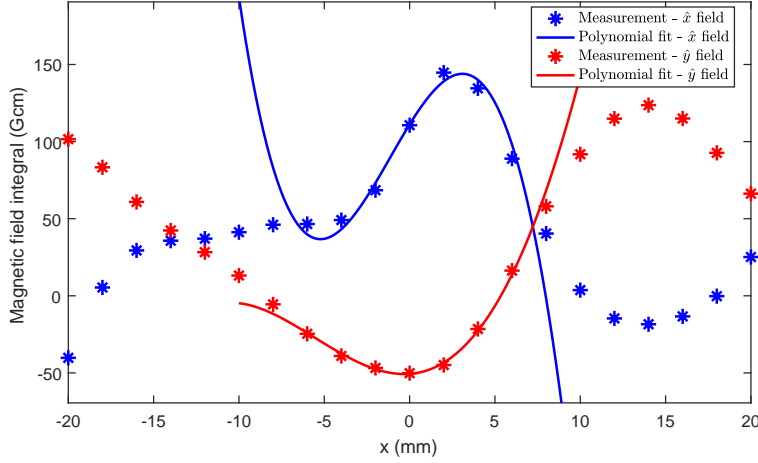


Figure 4.4: The wire scan measurements of FinEstBeAMS in vertical mode, showing the RFIs for different transverse positions. Both \hat{x} and \hat{y} are shown in blue and red. The blue and red lines correspond to a polynomial fit, heavily weighted around the middle points of the measurements.

time it took to change the coil currents from one outset value to the set point value was measured in order to allocate an appropriate amount of time for changing the coils during the correction measurements. The time delay between when a command was sent to the Tango server and the instant when Tango registered the command was also measured. This was done to get an estimate on the timescales where the Tango state is a reliable variable. These measurements were done 100 times for the FinEstBeAMS and SPECIES and the result is presented in Section 5.3. These results were needed to incorporate pauses in the code for an appropriate duration.

4.2.3 Feed Forward Measurements

The main objective of this project was to produce a table, with currents for the dipole corrector coils for every gap and phase, that keeps the orbit close to the golden orbit despite the effects of the ID. FinEstBeAMS was the first beamline on R1 to get a radiation safety permit. Hence this was the ID where the commissioning process started. After ironing out bugs in the code, the measurements of the correction currents for the helical mode of FinEstBeAMS were initialised. During the minimum gap measurements for large positive phases the vertical upstream corrector magnet was saturated. For minimum gaps at large negative phases the vertical downstream corrector was saturated. This was handled with the strategy presented in Section 3.4.2.

The measurement of the correction currents for the inclined mode was done next without saturation of any coil currents. With both operational modes done, a complete FFT for FinEstBeAMS was generated. The FFT was thereafter uploaded

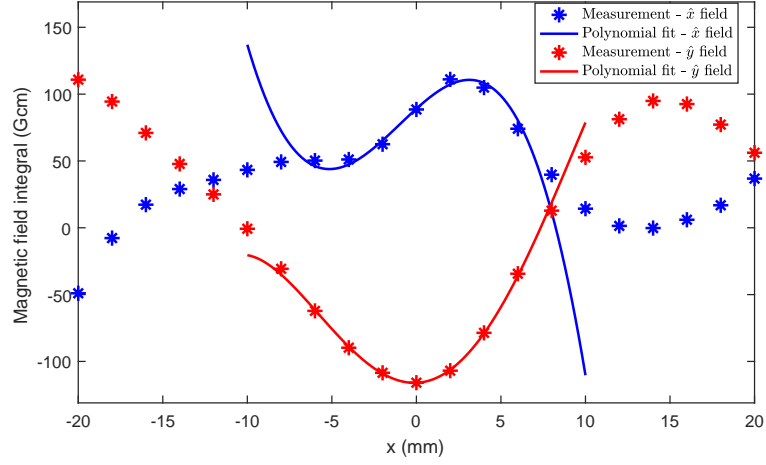


Figure 4.5: The wire scan measurements of FinEstBeAMS in circular mode, showing the RFIs for different transverse positions. Both \hat{x} and \hat{y} are shown in blue and red. The blue and red lines correspond to a polynomial fit, heavily weighted around the middle points of the measurements.

into the MAX IV feed forward system and a final verification of the FFT was performed when moving the ID gap and phase with this system enabled. After this, the ID was ready for beamline delivery.

4.2.4 Feed Forward Measurement Strategy (Pseudocode)

The desired output from the feed forward measurements is the corrector coil currents for each phase and each gap at both operational modes. The algorithm will be able to measure all phases and gaps for one operational mode in one run, in principle without supervision. The first algorithm developed is as follows:

1. Move to maximum gap and start phase
2. Correct the orbit (with SOFB)
3. Measure the orbit and set as golden orbit
4. Calculate a response matrix
5. Move to the next gap
6. Correct the orbit as close as possible to the orbit acquired in step number 3 using the response matrix calculated in step number 4 *
7. Save the current values of the corrector coils
8. Repeat from step number 5 until we are at minimum gap

*The accepted error rms was set to 1 μm . If this value is not reached, correction is tried up to 3 times whereupon the best solution is chosen.

9. Move to maximum gap
10. Move to next phase
11. Repeat from step number 5 until we have finished all phases
12. Feed Forward measurements are completed

This first algorithm did the job, but there were room for improvements. It was noticed that during the time of a complete measurement the orbit could *drift* i.e. the golden orbit measured half an hour ago is not necessarily the orbit current orbit of the bare lattice. The golden orbit thus needs to be measured more often, say at the start of each new phase. The response matrix did not completely correlate to the machine at lower gaps especially if the orbit had drifted. For this reason a recalculation of the response matrix was added to the strategy. It was realised that if the undulator moves in one big step from minimum gap to maximum gap, such as in step number 9, the beam could be disturbed or even lost because of the big magnetic differences of an open and closed gap. This was solved by implementing a function that stepped upwards through all gaps while applying the current values, that were measured on the way down and saved in step number 7.

The updated strategy is as follows with the updated parts in bold:

1. Move to maximum gap and start phase
2. Correct the orbit (with slow orbit feedback)
3. Measure the orbit and set as golden orbit
4. Calculate a response matrix
5. Move to the next gap
6. Correct the orbit as close as possible to the orbit acquired in step number 3 using the response matrix calculated in step number 4 *
7. **If the orbit is not satisfactory, calculate a new response matrix[†]**
8. Save the current values of the corrector coils
9. **If we are at a specific intermediate gap of 30 mm repeat from step number 4**
10. Repeat from step number 5 until we are at minimum gap
11. Move to maximum gap **applying the saved feed forward currents on the way up**
12. Move to next phase
13. Repeat from **step number 2** until we have finished all phases
14. Feed Forward measurements are completed

[†]I.e. when the error rms >10 μm .

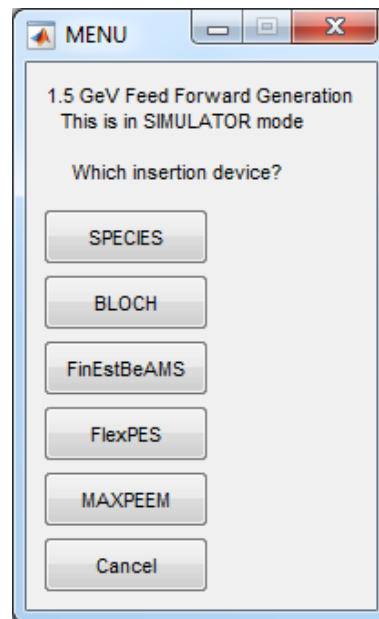


Figure 4.6: GUI for the selection of which ID that is to be commissioned.

4.2.5 Code implementation

When implementing the code for commissioning the undulator, a main goal has been to make everything general so that it can easily be adapted to any other ID on both R1 and R3. A clear folder structure based on which files contain hard coded values and machine specific information has been kept.

A simple Graphical User Interface (GUI) with selection buttons was implemented for the ease of use for operators when doing future commissioning. Some print screens of the GUI can be seen in Figure 4.6, 4.7, 4.8 and 4.9.

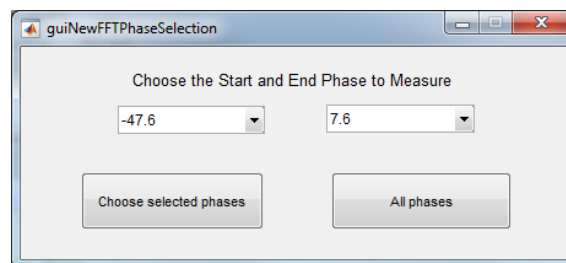


Figure 4.7: GUI for the selection of which phase interval that should be measured.

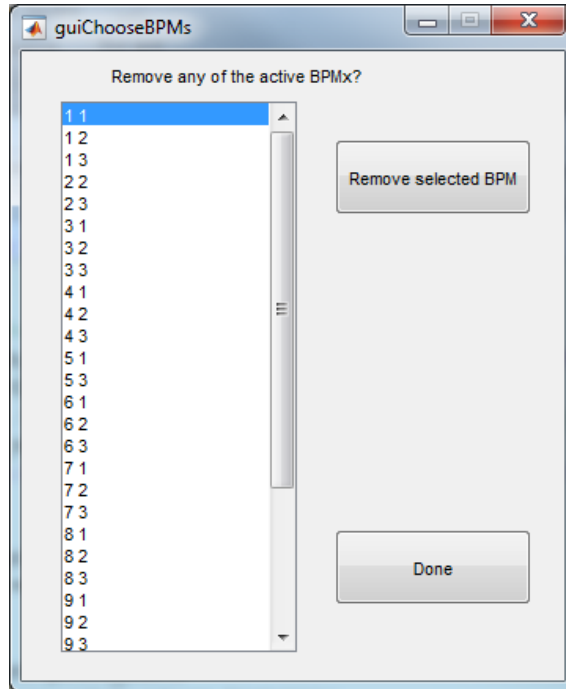


Figure 4.8: GUI for deselecting malfunctioning BPMs that are unwanted in the measurements.

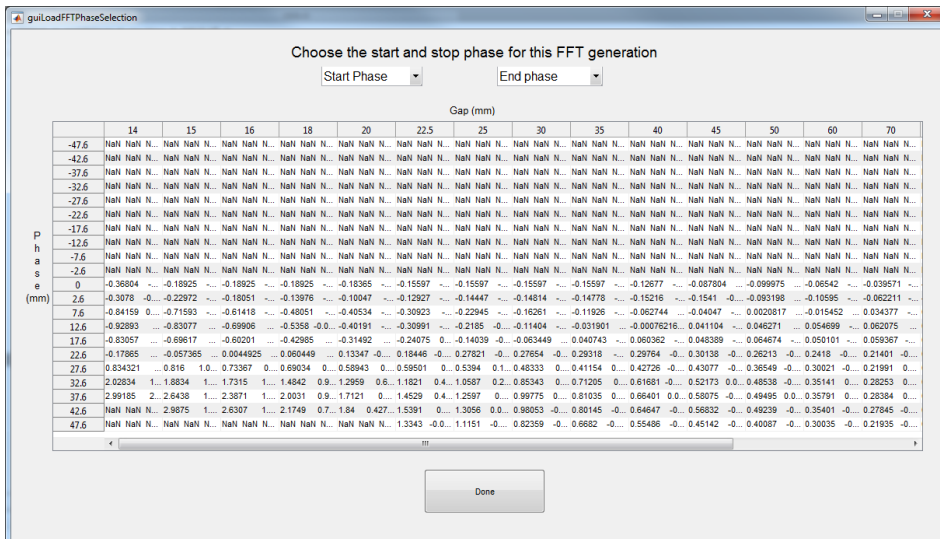


Figure 4.9: A view of which gaps and phases are already measured in a loaded feed forward table with the option of selecting which phases that should be filled in, in this run.

4.2.6 Determining Magnetic Field of the Corrector Coils

When saturation of the coils occurred for some gaps, the corrector coils were studied in order to compare them to their measured strength in bench measurements made prior to installation. To achieve this, a measurement of the orbit after a ± 1 A change of the corrector magnet current was made. Simulated orbits were then fitted to the measured orbits by varying the field integral of the simulated corrector coils in order to deduce the actual strength of the field produced by the corrector magnets.

4.2.7 Linear optics correction

In order to implement the LOCO method described in Section 3.4.3, two LOCO measurements were needed, one when the ID was at maximum gap and one when the ID was at the gap and phase that was to be corrected. Using the first LOCO measurement, the model lattice was changed to correspond better to the actual ring by allowing LOCO to adjust almost all of the variables. The improved model was thereafter used as the starting point for the LOCO algorithm with the later measurement as matching goal.

The initial attempt was to correct the linear optics using only the flanking magnets, i.e. the flanking quadrupoles and PFS's. When that was found lacking, all quadrupoles and PFS's were used in the correction.

For validating the results of the LOCO correction, the beta beat before and after correction is needed. Due to issues with the power supplies of the magnets, no corrections could be applied and the validation was instead done using a LOCO-fitted model. From this the expected beta beat after correction could be calculated.

4.2.8 Tune Measurement

The tunes were measured for FinEstBeAMS for the gaps of 20 mm and 15 mm at seven different equidistant phase values for inclined mode. For comparison the tune was measured with the ID at max gap. The design value of the tune was collected from the AT model.

5.1 Magnetic Bench Measurements

The integrated multipole components from the polynomial fits in Figures 4.4 and 4.5 as well as polynomial fits for the horizontal and inclined light polarisation modes are presented in Table 5.1.

The RFI values obtained from the magnetic bench measurements for $x = 0$, is presented in Table 5.2. The data in this table was extracted from Figures 4.4 and 4.5 depicting the wire scan measurements. An alternative method of obtaining these values is to integrate the Hall probe measurements along the whole ID in Figures 4.2 and 4.3. Note that the slight differences in Tables 5.1 and 5.2 are due to the former presenting data from the polynomial value at $x = 0$ and the latter is presenting the raw data points at $x = 0$.

Table 5.1: The components of the multipole expansion of the RFI in x and y of FinEstBeAMS. The components are the same as the integrated components B_{x0} , B_1 , B_2 e.t.c. from Equation 3.10 and 3.11. The tags *Horizontal*, *Vertical* e.t.c. refers to the polarisation of the light emitted (not to be confused with direction of the main magnetic flux density inside the ID).

	Dipole (Gcm)	Quadrupole (G)	Sextupole (G/cm)	Octupole (G/cm ²)
Horizontal RFI _x	-15.1	125	178	-295
RFI _y	9.79	-33.3	-63.7	85.9
Vertical RFI _x	111	179	-126.7	-363
RFI _y	-50.6	7.93	130	65.7
Circular RFI _x	89.1	114	-69.3	-238
RFI _y	-116	5.31	210	44.3
Inclined RFI _x	43.1	108	7.77	-242
RFI _y	-128	-23.6	195	56.5

Table 5.2: The RFI for $x = 0$ in \hat{x} and \hat{y} for four different modes.

	\hat{x}	\hat{y}
Horizontal	-17 Gcm	11 Gcm
Vertical	111 Gcm	-50 Gcm
Circular	89 Gcm	-116 Gcm
Inclined	42 Gcm	-128 Gcm

5.2 Simulated Orbit Correction

As described in Section 4.1.3 the orbit correction strategy was applied to the R1 AT model. The simulation got the horizontal orbit corrected to the goal orbit perfectly, as seen in Figure 5.1. The vertical orbit was corrected with similar accuracy. Before correction the simulated OD rms was $119 \mu\text{m}$ in x and $135 \mu\text{m}$ in y .

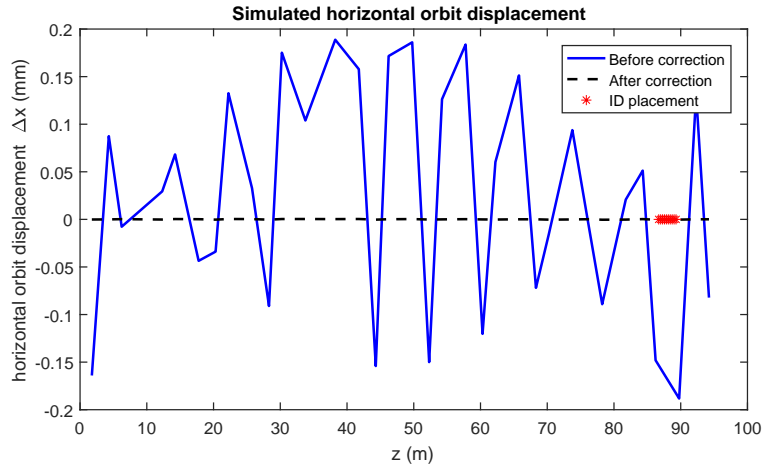


Figure 5.1: Simulated values of the horizontal orbit displacement from a model of the FinEstBeAMs ID. The blue line describes the beam kicked by the ID with a simulated field residual integral of 200 Gcm. The dashed black line is the displacement after correction, i.e. zero.

5.3 Corrector Coils

The coil strengths were measured and the maximum RFI was calculated, the results are seen in Table 5.3. There is a large difference in RFI of the vertical and horizontal coils.

The speed of current change was measured in the different undulators. The rate of change differed: a current change of 1 A for SPECIES' corrector magnets

Table 5.3: The RFIs for the different corrector coils measured at max current (-15 A) utilising electron beam displacement, and the design RFIs for open gap and an applied current of -15 A is compared.

	HU	HD	VU	VD
Measured RFI	578 Gcm	570 Gcm	218 Gcm	233Gcm
Design RFI	574 Gcm	527 Gcm	295 Gcm	300 Gcm

took 60 ms while FinEstBeAMS' took 1100 ms. FinEstBeAMS and Bloch have the same type of power supplies and coils so both should have the same speed.

5.4 Orbit Correction and Feed Forward Measurements

When not saturating a corrector, the OD correction strategy successfully achieved sub μm OD rms's at higher gaps and at most $4\ \mu\text{m}$ rms's for FinEstBeAMS at the lower gaps, i.e. the 14-20 mm gap region. When saturating one of the correctors, which only happened for some lower gaps, the modified strategy reduced the OD rms from at greatest $50\ \mu\text{m}$ to $20\ \mu\text{m}$ for FinEstBeAMS.

No OD was measured from open gap to minimum gap directly as this would be dangerous to the machine. The largest orbit displacement was seen when moving between the lower gaps, where the OD rms was at most $20\ \mu\text{m}$ after changing gap for the phases $\pm 40\text{ mm}$ in both helical and inclined mode. The corrector magnet currents that best corrected the orbit were saved to two FFTs, one for helical and one for inclined mode. The FFT currents were converted to RFIs using table 5.3. The horizontal corrector RFIs were summed for each operational mode and are presented in Figures 5.2 and 5.4. The same was done for the vertical correctors and the result can be seen in Figures 5.3 and 5.5.

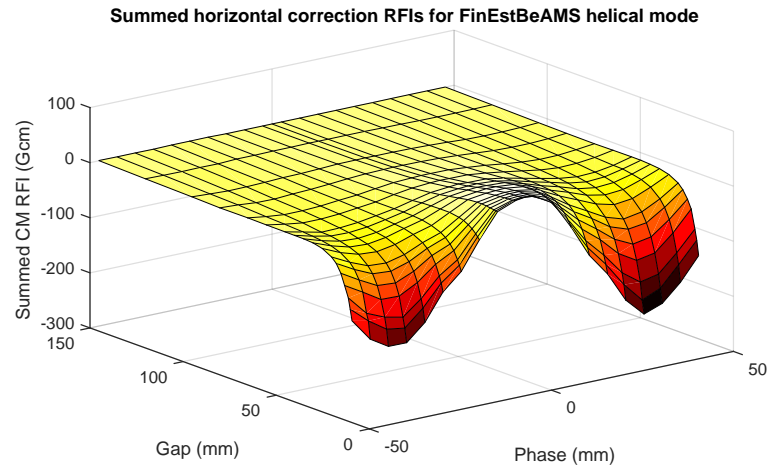


Figure 5.2: Total horizontal correction RFIs for FinEstBeAMS helical mode for gaps 14 mm to 150 mm and phases -46.7 mm to 46.7 mm.

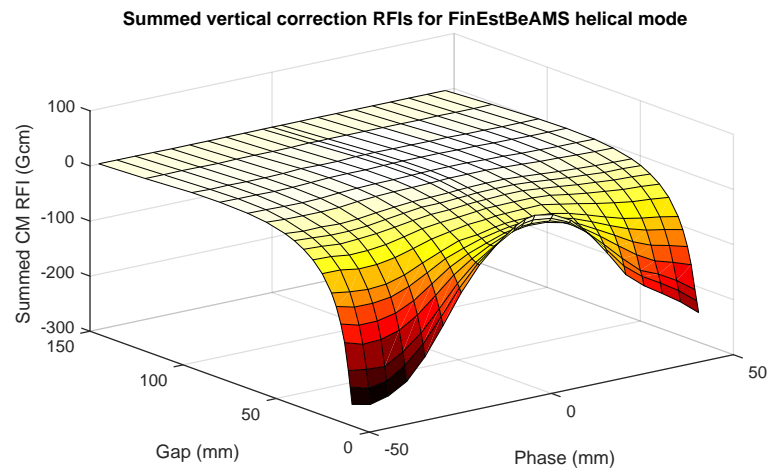


Figure 5.3: Total vertical correction RFIs for FinEstBeAMS helical mode for gaps 14 mm to 150 mm and phases -46.7 mm to 46.7 mm.

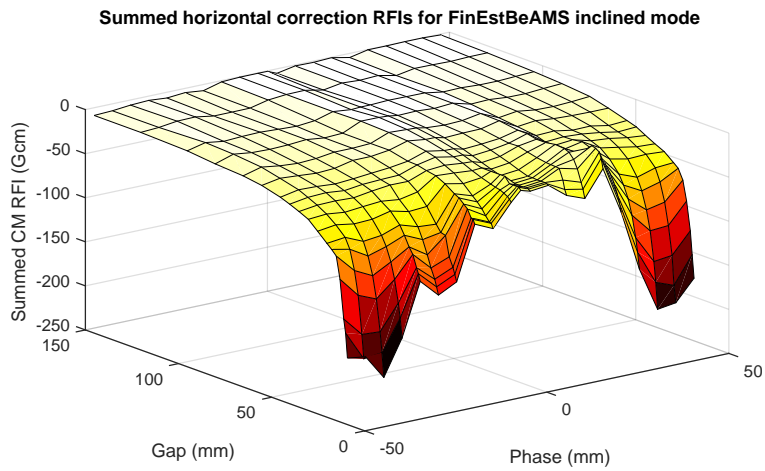


Figure 5.4: Total horizontal correction RFIs for FinEstBeAMS inclined mode for gaps 14 mm to 150 mm and phases -46.7 mm to 46.7 mm.

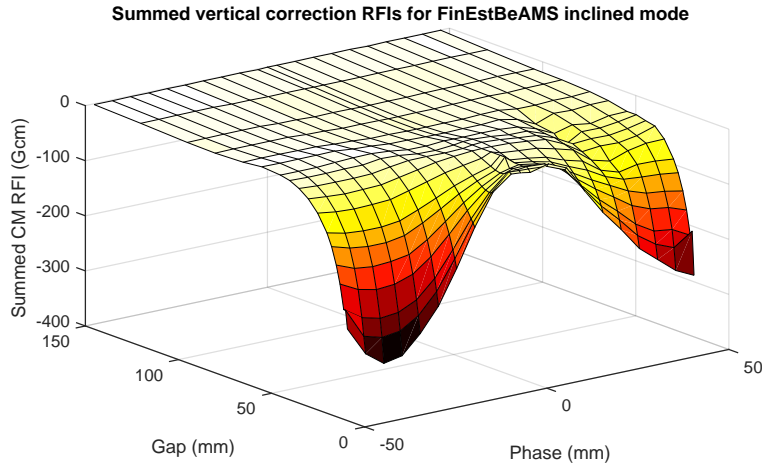


Figure 5.5: Total vertical correction RFIs for FinEstBeAMS inclined mode for gaps 14 mm to 150 mm and phases -46.7 mm to 46.7 mm.

A plot of the different individual corrector coil RFIs of FinEstBeAMS helical mode for all gaps and a specific phase can be seen in Figure 5.6.

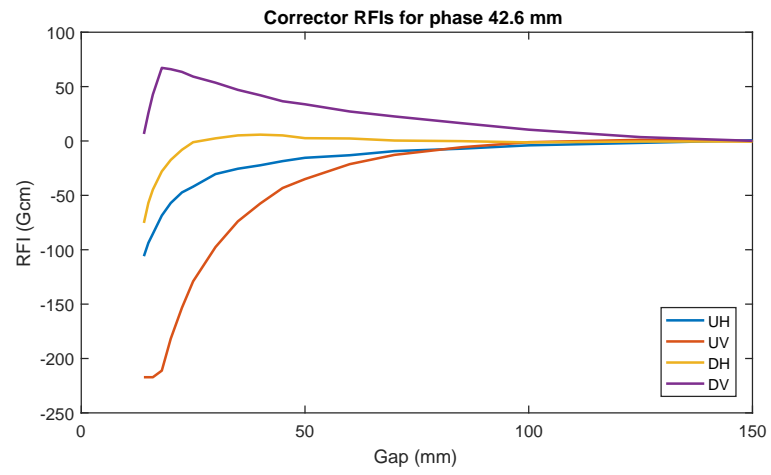


Figure 5.6: The FFT RFIs for all correctors at each gap measured in FinEstBeAMS helical mode, phase 42.6 mm.

5.5 Linear Optics Correction

The different simulated corrections of the linear optics (described in Section 4.1.4) gave the results that are seen in Figure 5.7 and 5.8. Only the beta beat is plotted but the corresponding AT model tunes and tune drifts can be seen in Table 5.4. One result not shown in the figures (in order to unclutter the plots) is that the beta beat increases from the uncorrected lattice to the ODC lattice, i.e. from active ID to active ID with orbit correction. When correcting with `fit tune` or LOCO, the beta beat goes down in both the horizontal and vertical plane, but to a greater extent in the horizontal plane.

Table 5.4: Tunes of the simulated machine in different stages of correction.

Lattice	Q_x	$\Delta Q_x/Q_{x_0}$	Q_y	$\Delta Q_y/Q_{y_0}$
Undisturbed lattice	11.2199	0 ppm	3.1500	0 ppm
ID disturbed lattice	11.2236	327 ppm	3.1479	-637 ppm
ODC lattice	11.2233	302 ppm	3.1482	-540 ppm
<code>fit tune</code> 2 corrected lattice	11.2200	3 ppm	3.1500	20 ppm
LOCO corrected lattice	11.2196	-28 ppm	3.1496	-111 ppm

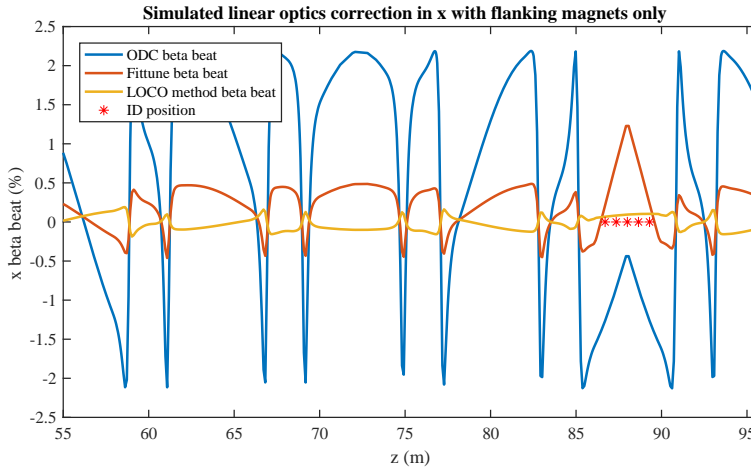


Figure 5.7: Simulated values of the horizontal beta beat before and after linear optics correction with the different methods.

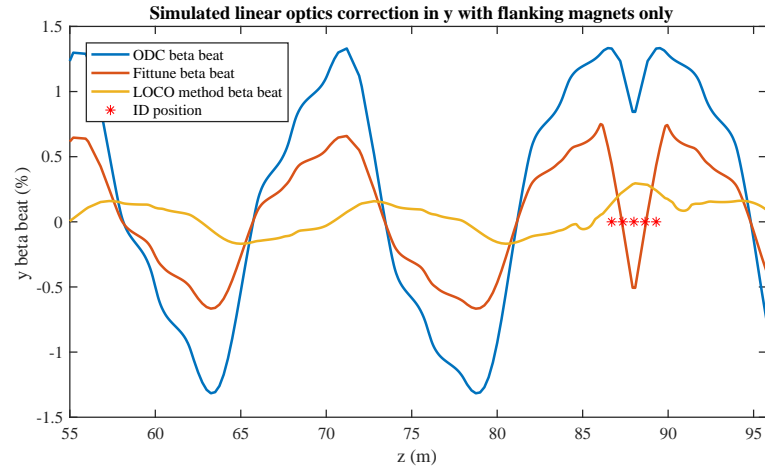


Figure 5.8: Simulated values of the vertical beta beat before and after linear optics correction with the different methods.

The beta beat from design values of R1 to R1 current working condition can be seen in Figure 5.9. This is the beta beat from the initial design model to the open gap model in figure 3.8.

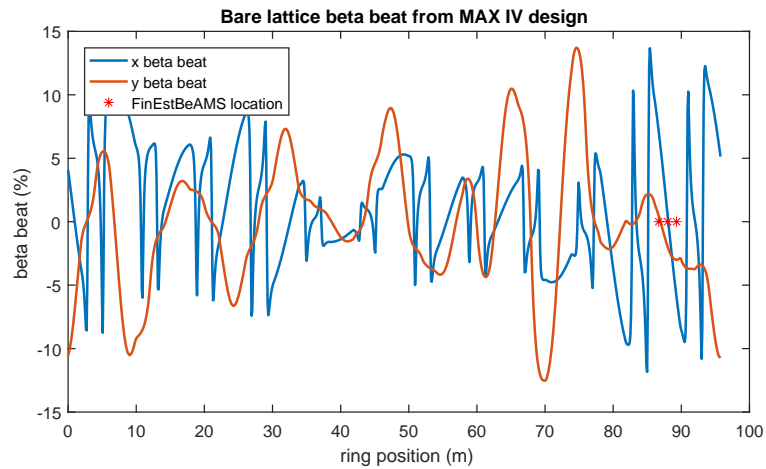


Figure 5.9: Beta beat of the bare R1.

As the currents to the quadrupoles on the real machine could not be changed, only the expected beta beat after correction could be studied. In Figures 5.10 and 5.11, the measured initial beta beat of FinEstBeAMS helical mode at closed gap and 0mm phase with OD correction is depicted with the expected beta beat after correction. The first strategy shown is using only the flanking PFS and quadrupole magnets to the FinEstBeAMS ID. The second strategy is using all PFS and quadrupoles in R1. The tunes calculated using AT in the different stages

are shown in Table 5.5.

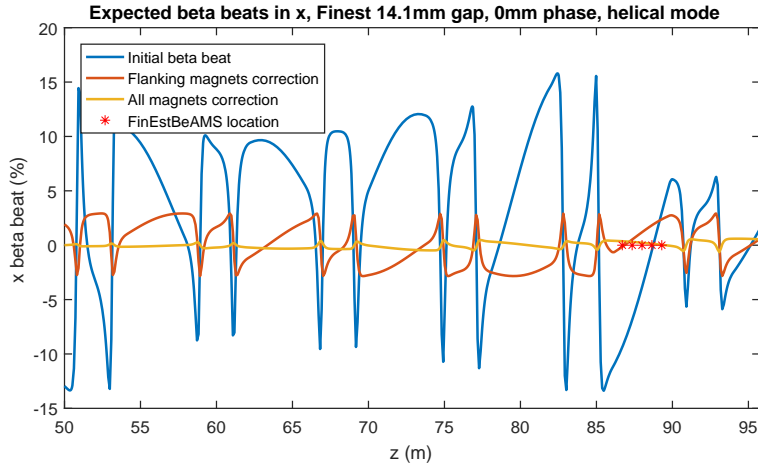


Figure 5.10: Initial and expected beta beat in x after linear optics correction for FinEstBeAMS at 14 mm gap and 0 mm phase in helical mode. The expected beta beat was calculated from a LOCO-fitted model of R1 at the specified gap and phase.

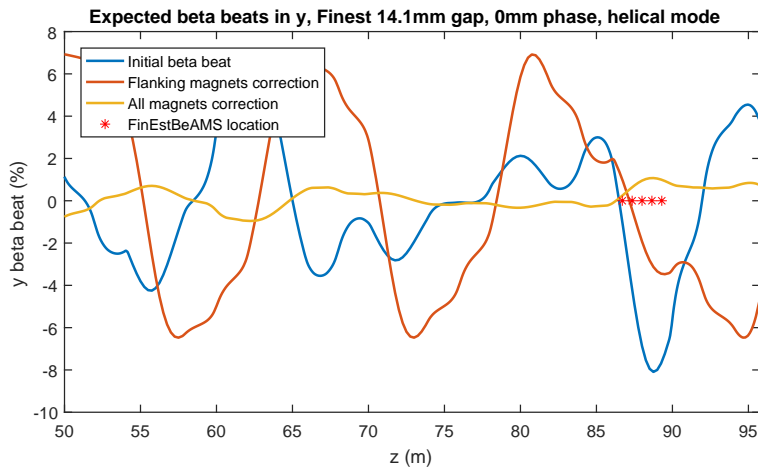


Figure 5.11: Initial and expected beta beat in y after linear optics correction for FinEstBeAMS at 14 mm gap and 0 mm phase in helical mode. The expected beta beat was calculated from a LOCO-fitted model of R1 at the specified gap and phase.

Table 5.5: Expected tunes using the AT toolbox before and after linear optics correction, FinEstBeAMS 14mm gap and 0mm phase in helical mode.

	Open gap	No linear optics correction	Flanking magnets correction	All magnets correction
Q_x	11.233	11.248	11.230	11.233
Q_y	3.160	3.176	3.173	3.167

5.5.1 Tune Measurements

The measured tunes in R1 while moving FinEstBeAMS to different gaps and phases are presented in Table 5.6. The measured tunes of the bare machine (FinEstBeAMS at maximum gap) was 11.2355 and 3.1376 in \hat{x} and \hat{y} respectively. The design values from the simulated lattice is 11.2199 and 3.14995.

Table 5.6: Tunes in R1 while moving FinEstBeAMS to different gap and phases, gap and phase is given in mm. The tunes are given in periods.

gap\phase	-47.6	-37.6	-27.6	0	27.6	37.6	47.6
20 mm - Q_x	11.174	11.191	11.228	11.246	11.231	11.193	11.174
Q_y	3.174	3.171	3.162	3.160	3.161	3.170	3.176
15 mm - Q_x	11.211	11.217	11.232	11.237	11.232	11.217	11.211
Q_y	3.154	3.153	3.151	3.145	3.151	3.153	3.154

5.6 Undulator Light Spectrum

The simulated light spectrum from FinEstBeAMS can be seen in Figure 5.12 where the flux is plotted for different photon energies. In Figure 5.13 the different harmonics are presented with energy and flux for varying gap of the ID.

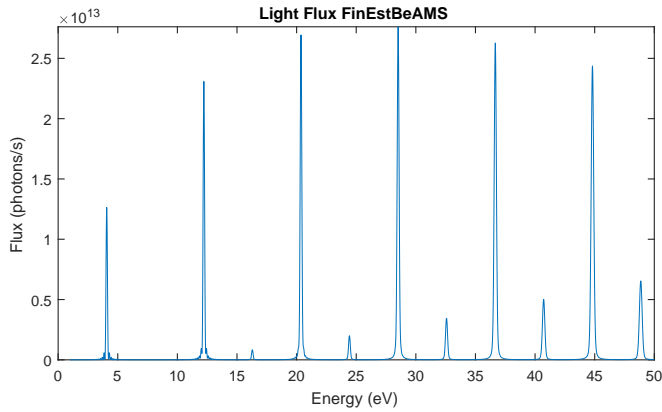


Figure 5.12: The simulated energy spectrum of light emitted from FinEstBeAMS at minimum gap in planar mode where the K value is 10.4. The first harmonic is at 4.1 eV, the even harmonics are not predominant especially for low harmonics as the observation angle is small. The flux is measured with a band width of 0.1% in a quadratic slit with 1 mm sides at a 14 m distance from the source, giving an observational angle of 0.07 mrad.

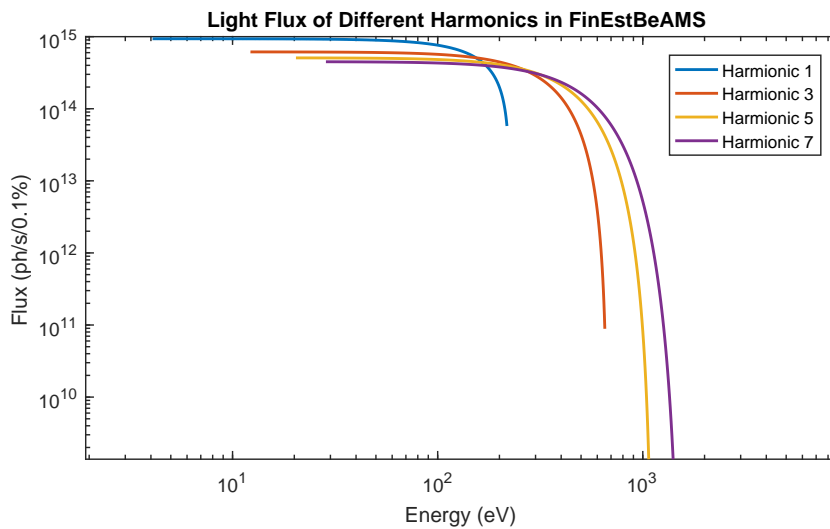


Figure 5.13: Simulated light emission showing energy and flux for each of the first odd harmonics at varying gaps of FinEstBeAMS, the lowest gap gives the highest flux and lowest energy for each harmonic.

6.1 Simulation Accuracy

The values for the total ID dipole strength used (i.e. 200 Gcm RFIs) in simulations were chosen before any analysis of machine measurements or magnetic bench measurements. As indicated by Figures 5.2 to 5.5, these simulation values are close to the real values of the ID at minimum gap for some phases.

Comparing the OD from the simulation to that of the machine at minimum gap is difficult, considering that during the generation of the FFT, the orbit was corrected in an iterative manner and never allowed to go over 50 μm . A comparison between the simulated OD rms ($\approx 100 \mu\text{m}$) and a rough estimation of the sum of the OD rms's observed after changing gaps ($\approx 10 \mu\text{m}$ between each gap, gap moved 18 times for every phase) indicates that the two are of the same order of magnitude.

The simulated quadrupole effect of the ID is not very accurate when comparing it directly to the magnetic bench measurements. For the horizontal mode, the greatest integrated quadrupole normal component RFI (RFI_x in Table 5.1) is 125 G. The same value in the simulation is $30 \text{ G/cm} \cdot 15 \text{ cm} = 450 \text{ G}$ (the quadrupole strength times the length of the magnet). As such, the simulated quadrupole strength is higher than what was measured prior to installation. The integrated quadrupole skew component (RFI_y in Table 5.1) is also non zero, which was assumed to be zero in the simulations. The beta beat of the real machine when at minimum gap is however much worse than in the simulation (comparing 2.5% to 15 % peaks in simulation and real machine). This difference could be due to the IDs intrinsic focusing effect not being displayed in the bench measurements. The reason that the intrinsic focusing is not measured with the wire scan is because it assumes a straight path through the center of the ID. The electrons however traverses the ID with an undulating path giving rise to these focusing effects. Another possible explanation for the difference is that the machine is operating far from its design beta function.

6.2 Magnetic Bench Measurements

Figure 4.2 and Figure 4.3 display the raw data from the Hall probe measurements. Calibration to suppress field coupling due to the Hall probe's rotational displacement is possible but has not been applied in this data set. This explains why the

vertical field component is non-zero in Figure 4.2. Analysis of the uncalibrated measurements is still interesting however. It can be seen that when the ID produces vertically polarised light the horizontal magnetic field is dominating, which is consistent with Equation 3.5. It can also be seen that in order to produce circular polarised light, the magnetic field components are equal in amplitude but different in phase, this is also consistent with basic theory of electromagnetism.

The magnetic bench measurements of FinEstBeAMS provided a $|RFI|$ from 11 Gcm to 128 Gcm close to minimum gap (see Table 5.2). The different dipole corrector magnets have maximum RFI values ranging from 218 Gcm to 578 Gcm (see Table 5.3). At a first glance at the results, this indicates that all orbit distortions that arise from the ID should be able to be corrected for. It is evident that this is not the case, considering the saturation issues at large phases and small gaps. Further, when correcting the orbit, it can be seen in Figures 5.2 to 5.5 that a RFI greater than the measured maximum of 128 Gcm was applied in order to correct for FinEstBeAMS's dipole effect. From Equation 3.34 it is known that the positional displacement caused by a dipole magnet depends on the beta function at the position of the magnet and the beta function at the points of measurement, i.e the BPMs. Since there is a 15% beta beat from the design values for the bare lattice, as seen in figure 5.9, this could also explain why the corrector magnets are underperforming - especially since the corrector magnets in question are located in a region with particularly bad beta beat (near FinEstBeAMS).

The explanation for RFIs being larger than measured is twofold. Since magnetic bench measurements were done with the ID at a different location and rotation, the geomagnetic field and other external magnetic fields are potentially not the same. The geomagnetic field is typically around 0.5 G and integrating this over the length of the ID gives a magnetic field integral of 130 Gcm which is on the same level as the total measured RFI of the ID. Further, when the ID was moved, slight shifts in magnet alignment can have occurred which would lead to slightly different performance. Considering that the field strengths of the permanent magnets in the ID are on the order of 1 T, an average change of 0.01% in field strength would yield an average residual field of 1 G, which in turn would yield a magnetic integral of 260 Gcm!

The second explanation why the electron beam measurements differ from the bench measurements is the high beta beat of the open gap machine. The magnetic measurements assumes a perfectly centred electron path inside the ID. If the trajectory goes off-axis inside the ID, it will experience another RFI as seen in Figures 4.4 and 4.5. Dipole fields inside the ID, that cancel each other in the wire scan measurement might not for the electron beam, due to the high beta beat of the bare machine. Instead for the electron beam, two opposite dipole fields with the same magnitude will only cancel each other out if they also are situated at positions with the same beta function values, as suggested by Equation 3.34. Furthermore, the bench measurements only indicate the angular displacement of the beam, not its positional. When the correction strategy tries to remedy a purely positional displacement, the sum RFI of the corrector magnets will be zero but the individual RFIs will have opposite signs. A large positional displacement coupled with angular displacement could then lead to the seen saturation. Evidence to that this is the case are the opposite signs of the vertical RFIs in Figure 5.6.

When the horizontal and vertical correction coils are compared in terms of the applied currents, Table 5.3, it is noted that the vertical coils use much higher currents to achieve the same RFI. As such, it is only the vertical corrector magnets that are saturated at different points in the feed forward generation. The vertical corrector coils are weaker by design due to the geometrical limitations as can be seen in Table 5.3. Also deducible by the table is that vertical correctors perform slightly below their design RFIs. This problem is connected to the corrector coil design in FinEstBeAMS and Bloch which is different from older IDs such as SPECIES. The apparent underperformance of the coils can also, as previously stated, be explained by the large beta beat of the bare machine.

In Table 5.2 it is noted that the RFI is much less in horizontal mode than the other operational mode. This is due to that this is the normal mode of operation of the ID, and thus the mode it has been optimised for.

6.3 Feed Forward Measurement

The main task of finding corrector coil currents correcting the orbit was achieved with very satisfactory results for all gaps, phases and operational modes. In the simulated case the results were perfect, but that is not possible in the real ring. Instead a rms of $< 1 \mu\text{m}$ was achieved for a majority of gaps and phases, which is close to the noise level of the BPMs (measured rms of BPMs is $0.4 \mu\text{m}$) and thus impossible to outperform. In the very few cases where one of the corrector coils were saturated the correction was still very successful. In these cases it was possible to correct the orbit to an error rms of $< 20 \mu\text{m}$ from an initial error rms of $50 \mu\text{m}$. This orbit displacement is well within the capabilities of the slow orbit feedback correction system. In Figure 5.6, the effect of the improved strategy can be seen as the vertical upstream corrector coil gets saturated at lower gaps. The vertical downstream corrector then starts compensating (its RFI decreases), keeping the sum of the RFI going in the same direction as suggested in the undeviating surface plot in Figure 5.3. If the bad state of the linear optics in the bare machine is the major reason for the underperformance of the vertical corrector coils, it is possible that saturation is a non-issue after the new linear optics equipment has been installed.

The results of the orbit correction were verified by putting the FFT of the measured data into a feed forward system which automatically updates the currents whenever the ID moves. The ID was then moved over to different phases and gaps while keeping an eye on the orbit to spot any displacement. This verification was successful and meant that the ID was ready for beamline delivery.

If any major change of the ID or R1 occurs in the future, the measured FFT becomes obsolete and a new FFT is needed. In anticipation of this, the measurement procedure was implemented so that it can be run completely with a GUI without knowledge of the underlying code. Further feed forward measurements on other IDs, not presently installed, will be relevant in the future. For this reason the code was written to be very easy to understand, with numerous comments and a description added for each function so that it could easily be adapted if needed.

6.4 Higher order correction

The feed forward table takes care of the position and angle displacements of the orbit, while the higher order magnetic effects, such as the quadrupole, sextupole and octupole elements of the ID, will largely remain uncompensated by the feed forward correction. These higher order magnetic fields affect the focusing, tune, and beta beat of the electron beam, as well as other effects not discussed in this thesis such as dispersion and chromaticity. Due to restrictions in what is possible to achieve with the machine at MAX IV as of the writing of this thesis report, the only higher order effect that was meaningful to analyse was the quadrupole effect, corresponding to the tune shift and beta beat.

In the first study of using correction by only using the flanking magnets, the simulations show that the beta beat is reduced from 2% to 0.5% in x and from 1.3% to 0.6% in y by the function `fit_tune2` while the LOCO method surpasses it by reducing the beta beat to roughly 0.3% in both x and y , as mentioned in Section 4.1.3. If minimising the beta beat is the goal, then from these simulations it was concluded that the LOCO method does just that without unnecessary sacrifice of the tune.

Due to the issues of the quadrupole power, forbidding any change in the power supplies to the quadrupole magnets, only analysis of the expected beta beat after correction can be performed. These results, seen in Figures 5.10 and 5.11, are promising as they show a reduction of beta beat peaks of 15% down to less than 1% in x . The reduction in y is less than this yet considerably better than with no correction. The expected correction results also show that for the current lattice, the method that uses only the flanking PFS and quadrupole magnets increase the beta beat in y , indicating that the method of using all magnets being the way to go. The expected tunes after correction using all magnets are also an improvement on having no correction, especially in x where the tune is returned to the open gap value as seen in Table 5.5.

After fixing the linear optics of R1, it would be interesting to see if the flanking quadrupole method becomes acceptable. It would also be interesting to see if, with a better R1 state, the location of the ID is as easily visible from the beta beat as it is in the simulations. Furthermore, can the bad tunes visible in Table 5.6 be brought back to the bare machine tune?

6.5 Undulator Light Spectrum

The light produced in FinEstBeAMS was simulated and is shown in Figure 5.12. Sadly, it was not possible to compare this simulated spectrum to the real spectrum from the device since no such spectrum is acquired at the time of the writing of this thesis. The first harmonic being at 4.1 eV for the minimum gap is however consistent with data found in the in-house FinEstBeAMS documentation. If the gap is increased the energy of the peak will increase while the flux will decrease, as indicated in figure 5.13. Since the light is measured in a small observational angle of 0.07 mrad, the even order harmonics are repressed.

Conclusion

The simulations with the used parameters were accurate enough to warrant doing them and provided a good basis for the measurements and analysis that followed.

The feed-forward tables were successfully generated and verified. This means that the ID is ready for beamline delivery. A general method of generating future FFTs has been developed and a handover process has been completed to MAX IV. Due to delays with radiation permits only one of the three originally planned IDs were possible to be commissioned, but since the methodology was developed in full, the theoretical and analytic depth of the report has not been affected.

The corrector coils were saturated at minimum gap for some phases. Worth noting is that this only occurred for a small minority of positions and will not considerably affect the end result, i.e. a functional ID. The saturation is suspected to occur because of a combination of two things. The horizontal correctors perform 25% below their design specification and the beta beat of the bare machine is at 15%, which is worse than anticipated.

In the rare cases where saturation occurs, the orbit correction could not be performed optimally. It is however within the margin where the OD can be corrected with the slow orbit feedback system. To produce an optimal FFT and to correct the orbit with minimum OD, either the vertical corrector coils should be replaced/adjusted so they perform according to specification or the linear optics could be adjusted to reduce the beta beat of the bare machine. As the correction is sufficient for beamline delivery this is not a pressing issue and the implementation of these improvements are not scheduled at this date.

A successful study of how the higher order correction should be applied has been completed, although it is not possible to verify the expected results in R1 because of temporary limitations (overheating of shunt resistances) in the hardware. This is instead left as future work together with the task of correcting for the ID's sextupole and octupole effect. Additional future work is the commissioning of the yet-to-be-installed IDs at MAX IV. The process is expected to be straightforward using the code developed in this thesis.

This is the first commissioning of an ID in R1, meaning that all these conclusions regarding the state of the linear optics, corrector coils, and the success of correcting the orbit have not been published before.

References

- [1] Sara Mikaelsson. *Commissioning and Characterization of Two Undulators at the MAX IV 3 GeV Storage Ring*. Master's thesis, Department of Electrical and Information Technology, Faculty of Engineering - LTH, Lund University, August 2016.
- [2] E. J. N. Wilson. Fifty years of synchrotrons. <http://accelconf.web.cern.ch/accelconf/e96/PAPERS/ORALS/FRX04A.PDF>.
- [3] Arthur L. Robinson. X-ray data booklet, October 2009.
- [4] Davide Castelvechi. Next-generation X-ray source fires up. <https://www.nature.com/news/next-generation-x-ray-source-fires-up-1.18253>, August 2015. Nature.
- [5] Elettra Sincrotrone Trieste. Apple II Undulator. <https://www.elettra.trieste.it/lightsources/fermi/fermi-machine/felundulator.html>, December 2017.
- [6] MAX IV. Alfresco document library. <http://alfresco.maxiv.lu.se>.
- [7] MAX IV Laboratory. *Strategy Report 2016-2026*, 2017.
- [8] MAX IV Laboratory. *Detailed Design Report MAX IV Facility*. Technical report, MAX IV, 2010.
- [9] Helmut Wiedemann. *Particle Accelerator Physics*. Springer International Publishing, 3 edition, 2007.
- [10] David J. Griffiths. *Introduction to Electrodynamics*. Prentice Hall, January 1999.
- [11] Klaus Wille. *The Physics of Particle Accelerators, an Introduction*. Oxford University Press, 2000.
- [12] Alice Hong. Dielectric Strength of Air. <http://hypertextbook.com/facts/2000/AliceHong.shtml>, 2000. The Physics factbook.

-
- [13] W. Eberhardt. Synchrotron radiation: A continuing revolution in X-ray science. *Journal of Electron Spectroscopy and Related Phenomena*, 200:31–39, 2015.
- [14] Pascal Elleaume. CERN Accelerator School, Lecture on: Insertion Devices. <https://cas.web.cern.ch/sites/cas.web.cern.ch/files/lectures/brunnen-2003/i.pdf>, 2003.
- [15] NIST. The NIST reference on Constants, Units, and Uncertainty. <https://physics.nist.gov/cuu/index.html>, October 2017.
- [16] Jeff Holmes, Stuart Henderson, Yan Zhang. US Particle Accelerator School, Lecture on: Transverse Beam Optics. <http://uspas.fnal.gov/materials/09VU/Lecture7.pdf>, 2009.
- [17] A. Terebilo. *Accelerator Toolbox for MATLAB*. Technical report, Stanford Linear Accelerator Center, Stanford University, Stanford, CA 94309 USA, May 2001. SLAC-PUB-8732.
- [18] A. Terebilo G. J. Portmann, J. Corbett. *Middle Layer Software Manual for Accelerator Control*, August 2006. LSAP-302.
- [19] MathWorks Inc. *mldivide*, \. <https://se.mathworks.com/help/matlab/ref/mldivide.html?requestedDomain=www.mathworks.com>, 2017.
- [20] Takashi Tanaka and Hideo Kitamura. Spectra: A synchrotron radiation calculation code. *Journal of synchrotron radiation*, 8:1221–8, December 2001.
- [21] Nicolas Leclercq. Tango controls, MATLAB bindings source code. <http://github.com/tango-controls/matlab-binding>, December 2016.
- [22] A. Terebilo. *ACCELERATOR MODELING WITH MATLAB ACCELERATOR TOOLBOX*. *Proceedings of the 2001 Particle Accelerator Conference, Chicago*, 2001.
- [23] J. Safranek. Experimental determination of storage ring optics using orbit response measurements. *Nuclear Instruments and Methods in Physics Research Section A: Accelerators, Spectrometers, Detectors and Associated Equipment*, 388:27–36, March 1997.
- [24] Greg Portmann, James Safranek, and Xiaobiao Huang. *Matlab based LOCO*. Technical report, SLAC, October 2011. SLAC-PUB 14640.

SVD and QR decomposition

A comparison was done between solving the corrector currents with the matlab backslash operator and singular value decomposition (SVD) which was implemented in the previous version of the algorithm. The MATLAB backslash operator solves the matrix equation using QR decomposition. Two corrector kicks will be determined for each axis, the SVD will thus only produce two singular values. The benefits of using SVD are then negated, as all singular values will have to be used.[19]

The relative error and time consumption of using both solvers were measured and is presented in Table A.1. The difference is in slight favour of using the backslash solver in both regards, hence it was used.

Table A.1: The root mean square (rms) error from the optimal solution is on the level of 5 nm with both solvers and the BPM noise level is on the level of 0.5 μm . Both perform significantly below the noise level in the simulated environment. The time difference is around 0.3 ms faster for the backslash operator.

	SVD	Backslash	Difference
rms error [mm]	$5.282\,997\,472 \cdot 10^{-6}$	$5.282\,997\,468 \cdot 10^{-6}$	$4.1 \cdot 10^{-15}$
time [s]	$7.9 \cdot 10^{-4}$	$4.5 \cdot 10^{-4}$	$3.4 \cdot 10^{-4}$

AT and MML

The main tool for simulating the electron beam in the 1.5 GeV storage ring is the accelerator toolbox (**AT**) for **MATLAB**. The toolbox was first developed at SLAC in tandem with the design of the SPERA3 light source and simulates particle motion using linear matrix elements[22]. What has made **AT** successful in the world of accelerator modelling is the relative ease to create new functions, the easy graphical visualisation of the results in **MATLAB**'s graphical interface and the growing number of toolboxes in **MATLAB** that can be used in tandem with **AT**.

In the **AT** simulation environment, each device along the accelerator structure, i.e. RF-cavities, bending magnets, quadrupoles, drift sections etc, are represented as an element with its own transfer matrix for either single particles or the Twiss parameters[17]. All these elements build up the *linear lattice*, or simply just called the lattice, which is a model of the entire accelerator structure, which in turn has more global properties. **AT** uses two global **MATLAB** structure array variables called **FAMLIST** and **THERING**, where the latter is a list of all the elements in the lattice and the former is a much shorter list containing all element families, i.e. the different elements that are found in the lattice[17].

Other than tracking individual particles, **AT** can also be used to model the linear optics of a lattice, i.e. how the beta functions behave. **AT** also handles chromaticity - the function that describes how the energy spread of the particles affect the particle beam. This property of **AT** is particularly useful for determining the linear optics of a real machine that is modelled in **AT** using LOCO (Appendix C).

The Matlab Middle Layer[18], **MML**, is a code interface used by the operators at MAX IV to control and analyse the machine. It lets the user work either in simulation mode or online mode. In the different modes, the user can with the same commands either talk to an **AT** model of the facility or the actual facility through the Matlab Tango Bindings.

The commands contained in the **MML** are for **getx** and **measloco** which returns the x orbit position at the active BPMs or performs a measurement of the data needed for running the LOCO algorithm (Appendix C). Not all devices in the facility are contained in **MML**, for instance insertion devices.

Linear Optics from Closed Orbits - LOCO

The beta function, i.e. the linear optics of the machine, cannot be known straight from the machine. Instead it must be gained through other means, the method for determining the linear optics of MAX IV and many other synchrotrons in the world is LOCO. LOCO has a few iterations but the version referred to in this thesis is a toolbox for MATLAB developed from the FORTRAN code with the same name used to analyse the NSLS X-Ray Ring at SLAC in the 1990's.[23]

Assuming a synchrotron ring has multiple corrector magnets used to fine-tune the orbit of the ring (at MAX IV the ones used for ID orbit correction are excluded for this), a response matrix for the effect of these correctors on the BPMs can be constructed. The basic premise of LOCO is that this response matrix, called \mathbf{R}_{meas} when measured on the real machine, is closely tied to the linear optics of the machine.[23]

As the same matrix can be calculated in an AT model of the machine, in that case called \mathbf{R}_{mod} , then if the two are matched similarly enough the linear optics of the model is in turn better matched to reality. The linear optics are then easily extracted using predefined functions in the AT toolbox. To achieve the matching, LOCO changes the parameters of the AT model using a Gauss-Newton minimisation algorithm and the user determines which parameters that are changed. The user may choose that the matching should be done by changing only the quadrupole component of some chosen magnets.

The mathematical formulation for comparing the two response matrices is

$$\chi^2 = \sum_{i,j} \frac{(R_{mod\ ij} - R_{meas\ ij})^2}{\sigma_i^2} \quad (C.1)$$

where σ_i^2 is the noise of the i -th BPM in the lattice.[24] For R1 there are roughly 35 correctors and 35 BPMs, resulting in a \mathbf{R}_{meas} and \mathbf{R}_{mod} being 35-by-35 sized matrices.

After running the LOCO-matching algorithm, the corrected model can be extracted and used in AT without issues. Using this model would then make other simulations of the accelerator structure more accurate.



LUND
UNIVERSITY

Series of Master's theses
Department of Electrical and Information Technology
LU/LTH-EIT 2018-620

<http://www.eit.lth.se>